The Astrophysical Journal, 988:169 (20pp), 2025 August 1 https://doi.org/10.3847/1538-4357/ade0b3

The Gravity Collective: A Comprehensive Analysis of the Electromagnetic Search for the Binary Neutron Star Merger GW190425

D. A. Coulter[1,2], C. D. Kilpatrick[3], D. O. Jones[4], R. J. Foley[2], J. Anais Vilchez[5], I. Arcavi[6], K. E. Clever[2], G. Dimitriadis[7], A. V. Filippenko[8], N. Muñoz-Elgueta[9], A. L. Piro[10], P. J. Quiñonez[2], G. S. Rahman[11,12], C. Rojas-Bravo[2], M. R. Siebert[1], H. E. Stacey[11], J. J. Swift[11], W. Zheng[8], J. S. Bloom[8], M. J. Bustamante-Rosell[2], K. W. Davis[2], J. Kutcka[2], P. Macias[2], P. McGill[2,13], E. Ramirez-Ruiz[2], K. Siellez[14], S. Tinyanont[15], S. B. Cenko[16,17], M. R. Drout[18], R. Hausen[19], D. Andrew Howell[20,21], W. V. Jacobson-Galán[8], D. Kasen[8,22], C. McCully[20], A. Rest[1,19], K. Taggart[2], and S. Valenti[23]

[1] Space Telescope Science Institute, 3700 San Martin Drive, Baltimore, MD 21218, USA; dcoulter@stsci.edu
[2] Department of Astronomy and Astrophysics, University of California, Santa Cruz, CA 95064, USA
[3] Center for Interdisciplinary Exploration and Research in Astrophysics (CIERA), Northwestern University, Evanston, IL 60201, USA
[4] Institute for Astronomy, University of Hawaii, 2680 Woodlawn Drive, Honolulu, HI 96822, USA
[5] Astronomy Center (CITEVA), University of Antofagasta, Avenida U. de Antofagasta, 02800 Antofagasta, Chile
[6] The School of Physics and Astronomy, Tel Aviv University, Tel Aviv 69978, Israel
[7] School of Physics, Trinity College Dublin, The University of Dublin, Dublin 2, Ireland
[8] Department of Astronomy, University of California, Berkeley, CA 94720-3411, USA
[9] Max-Planck-Institut fur Astrophysik, Karl-Schwarzschild-Str 1, D-85748 Garching bei München, Germany
[10] The Observatories of the Carnegie Institution for Science, 813 Santa Barbara St., Pasadena, CA 91101, USA
[11] Thacher Observatory, Thacher School, 5025 Thacher Rd. Ojai, CA 93023, USA
[12] Department of Mathematics and Computer Science, Wesleyan University, 45 Wyllys Ave, Middletown, CT 06457, USA
[13] Space Science Institute, Lawrence Livermore National Laboratory, 7000 East Avenue, Livermore, CA 94550, USA
[14] University of Tasmania, Physics, UTAS Physics Building - Private Bag 37, Hobart, Tasmania, 7001, Australia
[15] National Astronomical Research Institute of Thailand, 260 Moo 4, Donkaew, Maerim, Chiang Mai, 50180, Thailand
[16] Astrophysics Science Division, NASA Goddard Space Flight Center, Greenbelt, MD 20771, USA
[17] Joint Space-Science Institute, University of Maryland, College Park, MD 20742, USA
[18] David A. Dunlap Department of Astronomy and Astrophysics, University of Toronto, 50 St. George Street, Toronto, ON M5S 3H4, Canada
[19] Department of Physics and Astronomy, Johns Hopkins University, 3400 North Charles Street, Baltimore, MD 21218, USA
[20] Las Cumbres Observatory, 6740 Cortona Dr, Suite 102, Goleta, CA 93117-5575, USA
[21] Department of Physics, University of California, Santa Barbara, CA 93106-9530, USA
[22] Lawrence Berkeley National Laboratory, 1 Cyclotron Road, MS 50B-4206, Berkeley, CA 94720-3411, USA
[23] Department of Physics and Astronomy, University of California, Davis, CA 95616-5270, USA
Received 2024 April 23; revised 2025 May 29; accepted 2025 May 29; published 2025 July 23

Abstract

We present an ultraviolet to infrared search for the electromagnetic (EM) counterpart to GW190425, the second ever binary neutron star merger discovered by the LIGO-Virgo-KAGRA Collaboration. GW190425 was more distant and had a larger localization area than GW170817, so we use a new tool, `Teglon`, to redistribute the GW190425 localization probability in the context of galaxy catalogs within the final localization volume. We derive a 90th percentile area of 6688 deg^2, a $\sim$1.5$\times$ improvement relative to the LIGO/Virgo map, and show how `Teglon` provides an order-of-magnitude boost to the search efficiency of small ($\leqslant$1 deg^2) field-of-view instruments. We combine our data with a large, publicly reported imaging data set, covering 9078.59 deg^2 of unique area and 48.13% of the LIGO/Virgo-assigned localization probability, to calculate the most comprehensive kilonova (KN), short gamma-ray burst (sGRB) afterglow, and model-independent constraints on the EM emission from a hypothetical counterpart to GW190425 to date under the assumption that no counterpart was found in these data. If the counterpart were similar to AT 2017gfo, there would be a 28.4% chance of it being detected in the combined data set. We are relatively insensitive to an on-axis sGRB, and rule out a generic transient with a similar peak luminosity and decline rate as AT 2017gfo to 30% confidence. Finally, across our new imaging and publicly reported data, we find 28 candidate optical counterparts that we cannot rule out as being associated with GW190425, finding that four such counterparts discovered within the localization volume and within 5 days of merger exhibit luminosities consistent with a KN.

Unified Astronomy Thesaurus concepts: Neutron stars (1108); Black holes (162); Transient detection (1957); Astronomy software (1855); Gravitational waves (678); Astronomy databases (83)

Materials only available in the online version of record: machine-readable tables

1. Introduction

The mergers of neutron stars (NSs) and black holes (BHs) produce sufficiently strong gravitational waves (GWs) that they can be detected by modern interferometric instruments such as the Laser Interferometer Gravitational-wave Observatory (LIGO) and Virgo (B. P. Abbott et al. 2016a, 2016b, 2017a, 2017b, 2017c).

The majority of detected GW events involve binary black holes (R. Abbott et al. 2023), systems that are naively expected to produce no electromagnetic (EM) emission. However, the LIGO-Virgo-KAGRA (LVK) collaboration has detected nine mergers of compact binaries where at least one component has a mass consistent with being an NS (R. Abbott et al. 2021, 2023; A. G. Abac et al. 2024). In these cases, there is the potential for an electromagnetically luminous counterpart, such as as a short gamma-ray burst (sGRB) or a radioactively powered kilonova (KN; L.-X. Li & B. Paczyński 1998; M. Shibata & K. Taniguchi 2006; B. D. Metzger et al. 2010; L. F. Roberts et al. 2011; D. Kasen et al. 2017).

A single GW event, GW170817 (B. P. Abbott et al. 2017d), has been observed electromagnetically as GRB 170817A (A. Goldstein et al. 2017; V. Savchenko et al. 2017) and SSS17a/AT 2017gfo (D. A. Coulter et al. 2017). It was the result of the merger of two roughly equal-mass NSs with component masses of $1.46^{+0.12}_{-0.10}$ and $1.27 \pm 0.09\,M_{\odot}$ and a total mass of $2.73^{+0.04}_{-0.01}\,M_{\odot}$ (B. P. Abbott et al. 2017d). The ultraviolet (UV), optical, and infrared (IR; collectively denoted as UVOIR) data are consistent with a radioactively powered KN with $0.06\,M_{\odot}$ of ejecta that is rich in *r*-process material (I. Arcavi et al. 2017a; P. S. Cowperthwaite et al. 2017; M. R. Drout et al. 2017; M. M. Kasliwal et al. 2017; C. D. Kilpatrick et al. 2017; S. J. Smartt et al. 2017; M. Soares-Santos et al. 2017; S. Valenti et al. 2017). The gamma-ray burst (GRB) and its afterglow, observed as a nonthermal component for several years (D. Haggard et al. 2017; R. Margutti et al. 2017, 2018; A. Murguia-Berthier et al. 2017, 2021; K. D. Alexander et al. 2018; J. D. Lyman et al. 2018; M. Nynka et al. 2018; D. Pooley et al. 2018; J. J. Ruan et al. 2018; E. Troja et al. 2018, 2019, 2020; W. Fong et al. 2019; A. Hajela et al. 2019, 2022; L. Piro et al. 2019; S. Makhathini et al. 2021; C. D. Kilpatrick et al. 2022), are consistent with a structured jet having an opening angle $\theta_j \approx 5^{\circ}$ pointed $\sim 20^{\circ}$ from our line of sight.

Localizing new EM counterparts to GW events has been a major focus of GW astronomy since 2017. While GW events up through LVK observing run 4a (O4a; R. Abbott et al. 2021, 2023; A. G. Abac et al. 2024) have been localized to a precision of (at best) tens of square degrees, arcsecond localizations of their EM counterparts are necessary to enable analysis of their host environments, the mechanisms that power their GRB and KN emission, and new studies in cosmology and NS physics that require both GW and EM emission. For example, simultaneous detection of NS mergers in GW and EM emission have led to new constraints on the nuclear equation of state (C. D. Capano et al. 2020), studies of the nature of gravity (T. Baker et al. 2017), analysis of NS merger populations in the local Universe to compare with GRBs discovered at redshift $z > 0.1$ (W. Fong et al. 2017; W.-f. Fong et al. 2022; A. E. Nugent et al. 2022), a novel method to measure the Hubble constant (B. P. Abbott et al. 2017e), and analysis of the sites and mechanisms for *r*-process production (P. S. Cowperthwaite et al. 2017; M. R. Drout et al. 2017; M. M. Kasliwal et al. 2017; C. D. Kilpatrick et al. 2017; S. J. Smartt et al. 2017).

Of the eight compact-binary mergers that the LVK has detected through its third observing run (O3), five have one component that is consistent with that of a BH (i.e., a neutron star–black hole merger, NSBH) and a mass ratio where the secondary component (if an NS) is expected to be disrupted inside the innermost stable circular orbit, precluding any EM emission (see, e.g., E. Nakar 2020; F. Foucart 2021).

Besides GW170817, the only other binary neutron star (BNS) merger yet detected is GW190425, which consisted of a $2.02^{+0.58}_{-0.34}$ and $1.35 \pm 0.26\,M_{\odot}$ NS with a total mass of $3.4^{+0.3}_{-0.1}$ $M_{\odot}$ (B. P. Abbott et al. 2020a). Unfortunately, GW190425 was a "single-detector" event, only observed by the LIGO Livingston detector. Consequently, its initial (final) localization was constrained to 10,183 $\deg^2$ (9881 $\deg^2$) at 90% confidence, covering roughly a quarter of the sky. Additionally, its high total mass implies a KN that is fainter and redder than AT 2017gfo (R. J. Foley et al. 2020). Because a large fraction of the localization region was close to the Sun, no observatory could practically observe the entire localization region. Moreover, the size of the localization region and its extent over both hemispheres meant multiple telescopes were necessary to cover the maximum area possible.

Starting 15.5 hr after the trigger, we observed portions of the GW190425 localization region using five small-aperture telescopes as part of the One-Meter, Two-Hemispheres (1M2H) team. At the same time, several other teams, including GRANDMA, GROWTH, GOTO-4, SAGUARO, and others, began their own observing campaigns (M. W. Coughlin et al. 2019; G. Hosseinzadeh et al. 2019; M. J. Lundquist et al. 2019; S. Antier et al. 2020; B. P. Gompertz et al. 2020; R. L. Becerra et al. 2021; S.-W. Chang et al. 2021; G. S. H. Paek et al. 2024; S. J. Smartt et al. 2024). Each facility has different capabilities in aperture, field of view (FOV), and location. Additionally, strategies related to choosing pointings, filters, and cadence resulted in a heterogeneous but vast data set. No candidate counterpart has been reported with high confidence in these data (though see A. Moroianu et al. 2023, for discussion of a low-significance fast radio burst counterpart), and the possible emission from a KN or sGRB has been limited by the multiple analyses from the above individual teams on their separate data sets.

In this work, we seek to address these limitations by combining publicly reported, disparate data sets, including our own newly reported UVOIR search for an EM counterpart, into a single, comprehensive data set that is analyzed in a self-consistent manner. To perform such an analysis, we have developed a tool called `Teglon` which combines these data and also leverages our knowledge of the three-dimensional (3D) locations of galaxies to redistribute the original LVK-assigned GW probability to regions (and corresponding covering observations) where a counterpart was likely to be found.

We describe this combined data set in Section 2, and our detailed candidate vetting process is discussed in Section 3. We introduce `Teglon` (D. A. Coulter et al. 2025, in preparation; D. A. Coulter 2021),[24,25] our new, open-source tool for analyzing EM search data and performing pixel-level upper-limit calculations, in Section 4. In Section 4.1, we describe how `Teglon` is used to perform a sophisticated joint analysis of the imaging data from publicly reported observations and data newly reported here. We account for the recovery of artificial sources in each image (when available), line-of-sight extinction, the 3D probability from GW data, and available galaxy catalogs and their 3D completeness. From this

[24] https://github.com/davecoulter/teglon_O4
[25] https://anathem.fandom.com/wiki/Teglon

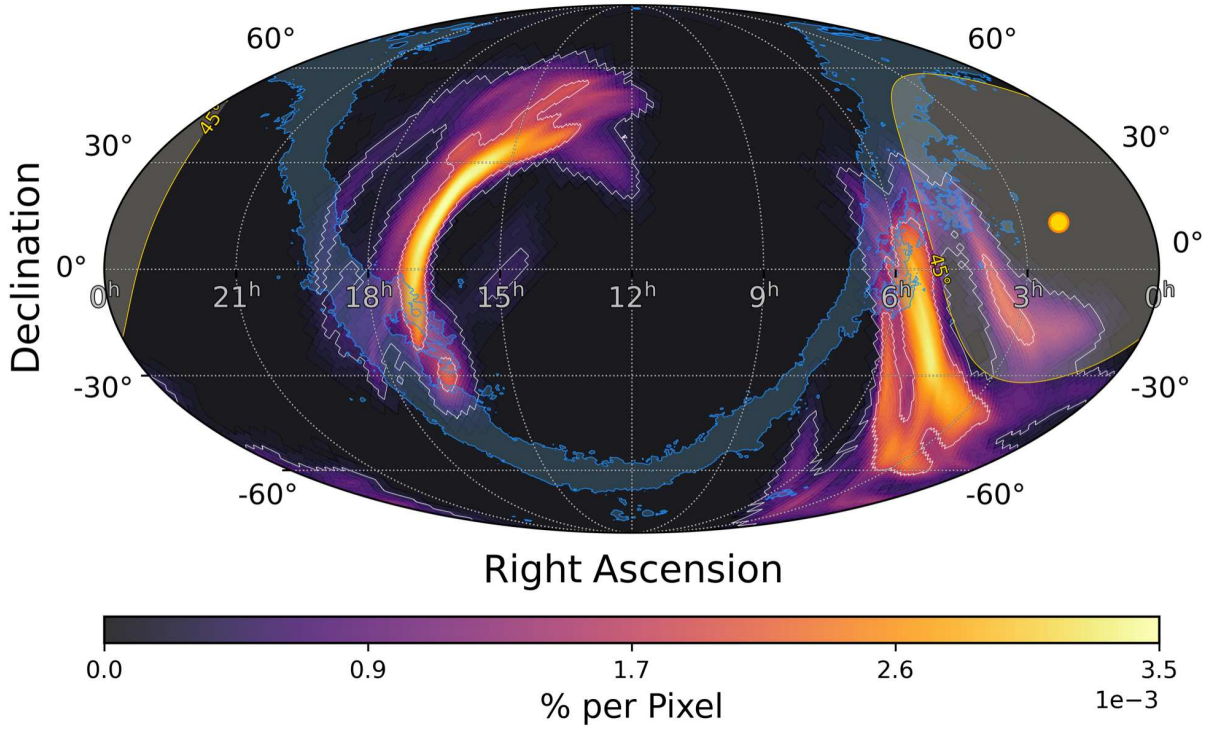

Figure 1. The LVK localization region for GW190425. Contours correspond to the 50th (2400 deg^2) and 90th (9881 deg^2) percentile regions. In blue is the contour corresponding to the Milky Way r-band extinction of 0.5 mag. Near 3 hr of R.A. is the location of the Sun on 2019 April 25, with a yellow Sun separation contour of 45°.

analysis, we present in Section 5 joint KN, sGRB, and model-independent constraints on the UVOIR emission from GW190425 under the assumption that no counterpart to GW190425 was found. Section 6 discusses these results in the context of the LVK's current (i.e., fourth, O4) and future observing runs (O5+), and how future observational campaigns can adjust to improve our chances of discovering the next GW counterpart, along with a broader discussion of our analysis methods and prospects for improving the localizations of GW events based on contextual data.

Throughout this paper, UTC dates are used, all magnitudes are reported in AB mag (J. B. Oke & J. E. Gunn 1983), and we adopt a flat ΛCDM cosmology with the following parameters: $H_0 = 100\,h = 70$ km s^{-1} Mpc^{-1}, $\Omega_{\rm M} = 0.27$, and $\Omega_\Lambda = 0.73$.

2. Observations

GW190425 (denoted as S190425z by LIGO Scientific Collaboration & Virgo Collaboration 2019) was initially reported to have a BAYESTAR (L. P. Singer & L. R. Price 2016) 90% credible localization of 10,183 deg^2 and a luminosity distance of 155 ± 45 Mpc. These were later refined to a final localization of 9881 deg^2 and a luminosity distance of 159^{+71}_{-69} Mpc (Figure 1; B. P. Abbott et al. 2020a). Because of this large area, we consider any data accessible across the sky relevant if obtained within 2 weeks of 2019 April 25, including all available targeted search data for GW190425 in Treasure Map (TM; S. D. Wyatt et al. 2020). This comprises imaging data for GW190425 from the 1M2H Collaboration, from Gravity Collective (GC) partners Las Cumbres Observatory (LCO) and the 0.76 m Katzman Automatic Imaging Telescope (KAIT; A. V. Filippenko et al. 2001) at Lick Observatory, from publicly reported limits through the TM application (S. D. Wyatt et al. 2020), and from the literature and private communication for the Pan-STARRS and ATLAS telescopes. These TM data include limits for both GW events from the Zwicky Transient Facility (ZTF; E. C. Bellm et al. 2019), the Gravitational-wave Optical Transient Observer 4 telescope (GOTO-4; D. Steeghs et al. 2022), the Swift Ultra-Violet/Optical Telescope (P. W. A. Roming et al. 2005), the MLS 10K charge-coupled device (CCD) camera via the Catalina Sky Survey (CSS; E. Christensen et al. 2018), and the MMTCam via the Fred Lawrence Whipple Observatory (G. G. Williams 2018). In addition to these targeted search data, we include untargeted imaging data across all 1M2H telescopes, collecting a total of 3598 public and private pointings for this analysis, which cumulatively cover 48.13% of the two-dimensional (2D) probability and 48.28% of the Teglon-redistributed probability (see Sections 4 and 4.1) from the final maps presented by B. P. Abbott et al. (2020a).

2.1. One-Meter Two-Hemispheres Data

The 1M2H Collaboration was established in 2017 and originally used two 1 m telescopes, the Nickel telescope at Lick Observatory in California and the Swope telescope at Las Campanas Observatory in Chile, to search for EM counterparts to GW sources. In 2019 this collaboration was expanded to include the 0.7 m robotic Thacher telescope at the Thacher School Observatory in Ojai, California (J. J. Swift et al. 2022), and the A Novel Dual Imaging Camera (ANDICAM; D. L. DePoy et al. 2003) on the SMARTS 1.3 m telescope at Cerro Tololo Interamerican Observatory, Chile. We present data from this collaboration for the first time, and describe our reduction process and limits below.

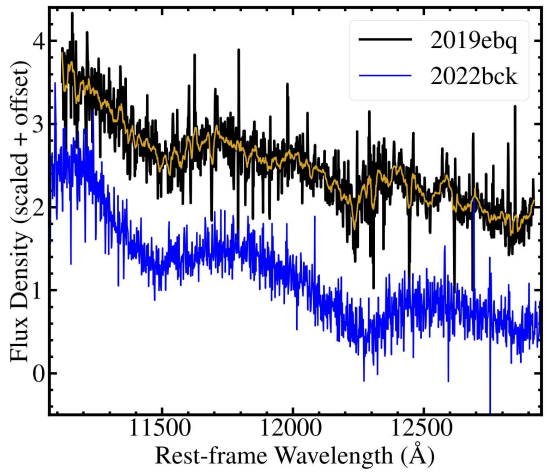

Figure 2. MOSFIRE NIR spectrum of SN 2019ebq (black), covering the *J* band blueward of 12900 Å, obtained on 2019 April 26, 14:32:11 on Keck I. The spectrum has been smoothed to a resolution of 17 Å (yellow) for analysis of the broad transient features present at these wavelengths. Our SN 2019ebq MOSFIRE spectrum appears consistent with a Type Ib/c SN, and is therefore unrelated to the GW event (see Section 2.1.5; G. Dimitriadis et al. 2019). We demonstrate this point by comparing it to a Keck/NIRES spectrum of the Type Ib SN 2022bck presented by S. Tinyanont et al. (2024). The similarity between these spectra reinforces the nature of this object as an SN and not a GW counterpart.

2.1.1. ANDICAM

We observed galaxies in the localization region of GW190425 with ANDICAM. All observations were performed on 2019 April 25–26 as described in Table 1. ANDICAM enables simultaneous optical observations using a CCD with a $10' \times 10'$ FOV and IR observations using an array with a $3.'3 \times 3.'3$ FOV. We searched the initial localization with the CCD and IR detectors to obtain *I*- and *H*-band observations of 25 galaxies within the GW190425 90th percentile localization region, and followed two optical candidates with a combined CCD+IR filter set of *I*, *J*, *H*, and *K*. All images for the CCD and IR detectors were reduced using `photpipe` (A. Rest et al. 2005), including bias subtraction, dark corrections for the IR detector, and flat-fielding. The images were aligned using Gaia astrometric standards (Gaia Collaboration et al. 2021). We then performed photometry in each image using `DoPHOT` (P. L. Schechter et al. 1993). Finally, the images were flux-calibrated using Pan-STARRS Data Release 2 (DR2) photometric standards (H. A. Flewelling et al. 2020) transformed into the *I* band (following transformations by S. Jester et al. 2005) and Two Micron All Sky Survey (2MASS) *H*-band standards (M. F. Skrutskie et al. 2006). We obtained follow-up observations of each field to use as templates for subtraction on 2019 June 5–11. After processing each image using the methods mentioned above, we subtracted the reference images from our science frames using `HOTPANTS` (A. Becker 2015). Final photometry for all transient sources in each difference image was obtained using a custom version of `DoPHOT`.

2.1.2. Nickel

We observed galaxies in the localization region of GW190425 with the Direct 2k × 2k ($6.'8 \times 6.'8$) camera on the Nickel 1 m telescope at Lick Observatory, Mt. Hamilton, California. We performed targeted observations of candidate host galaxies in the *r* band from 2019 April 26 to 2019 May 9, and we include in our analysis untargeted *BVri* observations in the same date range that are also within the GW190425 90th percentile localization region. All observations were reduced following the procedure described above for ANDICAM CCD imaging, including image subtraction with templates obtained from 2018 April 22 to 2020 May 10 and forced photometry on all candidate optical counterparts using `DoPHOT`.

2.1.3. Thacher

We observed GW190425 with the Andor 2k × 2k camera ($20.8' \times 20.8$) on the 0.7 m robotic Thacher telescope at the Thacher School Observatory in Ojai, California (J. J. Swift et al. 2022). We include *griz* follow-up data targeting the 90th percentile localization region of GW190425 obtained from 2019 April 26 to 2019 May 4. All imaging was reduced following the aforementioned methods and by C. D. Kilpatrick et al. (2021a). Template imaging of each field was obtained from 2019 February 23 to 2021 August 6. Our final observation list is given in Table 1.

2.1.4. Swope

We observed the localization region of GW190425 with the Direct 4k × 4k camera ($29.'8 \times 29.'7$) on the 1 m Swope telescope at Las Campanas Observatory, Chile. Our Swope observations consisted of targeted observations within the 90th percentile localization region of GW190425 in the *i* band obtained from 2019 April 25 to 2019 May 9 and untargeted *uBVgri* observations within the same area and time frame. These data were reduced following the ANDICAM/CCD procedures described above. We obtained template imaging from 2018 August 16 to 2020 February 25 to perform image subtraction in each frame and search for optical transients, and to generate forced photometry on known optical transients in each image.

2.1.5. SN 2019ebq and MOSFIRE

We obtained near-infrared (NIR) spectra of the candidate counterpart to GW190425 SN 2019ebq on 2019 April 26, 14:32:11 with the Multi-Object Spectrometer For Infra-Red Exploration (MOSFIRE; I. S. McLean et al. 2012) on the Keck I 10 m telescope. The spectrum was originally reported and described by G. Dimitriadis et al. (2019). We reduced the spectrum following standard procedures using `spextool`, and show the final reduced spectrum in Figure 2. Similar to findings by G. Dimitriadis et al. (2019) and M. Nicholl et al. (2019), we classify this source as a Type Ib/c supernova (SN Ib/c) near peak light based on comparison to a Keck/NIRES spectrum of the Type Ib SN 2022bck presented by S. Tinyanont et al. (2024).

2.2. Gravity Collective Data

2.2.1. KAIT

The 0.76 m KAIT (M. Richmond et al. 1993; A. V. Filippenko et al. 2001) at Lick Observatory targeted galaxies in the localization regions of GW190425 between 2019 April 25 and 27, as described by W. Zheng et al. (2019). Galaxies were selected from GLADE (G. Dálya et al. 2018) according to their *B*-band luminosity, with target priority reweighted by elevation at the time of observation. All observations were performed in a "Clear" filter. Between both events, 688 galaxies were targeted,

with all fields being reimaged in 2023 July to provide templates of the same fields for detailed analysis. Following standard imaging and photometry procedures (e.g., M. Ganeshalingam et al. 2010; W. Zheng et al. 2017), the images were calibrated, and point-spread function (PSF) photometry was performed using DAOPHOT (P. B. Stetson 1987) in IDL. The throughput of the KAIT "Clear" filter is close to that of the *R* band (W. Li et al. 2003), so local AAVSO Photometric All-Sky Survey standards (A. A. Henden et al. 2015) were transformed to the A. U. Landolt (1992) *R* band following S. Jester et al. (2005). Template images were then subtracted from the August 15 and 18 epochs using a custom IDL-based image-subtraction pipeline for PSF convolution. Finally, we estimate the limiting magnitude in each subtracted image using the flux-weighted average of the sky background in the convolved science and template frames, which is reported in Table 1.

2.2.2. LCO

The GC combines follow-up efforts by 1M2H and the LCO Global Telescope network (T. M. Brown et al. 2013), which includes 14 0.7–1 m telescopes distributed worldwide. LCO observed the localization region of GW190425 with a galaxy-targeted search and prioritization strategy described by I. Arcavi et al. (2017b). For both GW events, LCO obtained 773 exposures of 300 s duration each in *gri* using the Sinistro cameras ($26' \times 26'$ FOV) mounted on these telescopes (I. Keinan & I. Arcavi 2025). Image processing was performed by the LCO BANZAI pipeline (C. McCully et al. 2018), and limiting magnitudes were calculated using LCOGTSNpipe (S. Valenti et al. 2016). Sloan Digital Sky Survey (SDSS; K. N. Abazajian et al. 2009), PS1 (H. A. Flewelling et al. 2020), or Dark Energy Camera (T. M. C. Abbott et al. 2018) template images were used in the science image bands to perform image subtraction using PyZOGY (B. Zackay et al. 2016; D. Guevel & G. Hosseinzadeh 2017). The limiting magnitudes were calculated by determining the Poisson noise due to the sky using the median absolute deviation of the entire image. The Poisson and read noise were combined, and the 3σ limiting magnitude (median limiting magnitude of 22.1 mag) was estimated by inverting the standard signal-to-noise ratio (S/N) equation.

2.3. Public Data via Treasure Map

2.3.1. ZTF

ZTF is a 47 $\deg^2$ FOV optical instrument on the Palomar 48 inch Schmidt telescope (E. C. Bellm et al. 2019). We include 313 ZTF pointings reported to TM with a status of "completed" for GW event GW190425, and whose image-reduction process is outlined by M. W. Coughlin et al. (2019). Pointings span the *g*, *r*, and *i* bands, with a median *r*-band depth of $\sim$21.5 $m_{\rm AB}$. Within TM, each pointing includes the central coordinate of the FOV, filter, MJD of the observation, and limiting AB magnitude.

2.3.2. CSS

CSS operates the MLS 10k CCD camera on the Mt. Lemmon 1.5 m telescope, which has a $\sim$5 $\deg^2$ FOV and was used by the Searches after Gravitational Waves Using ARizona Observatories (SAGUARO) team to search for 17 GW events within O3 (M. J. Lundquist et al. 2019; K. Paterson et al. 2021). We include 61 pointings taken in an open filter to a median limiting mag of $\sim$21.3 $m_{\rm AB}$.

2.3.3. GOTO-4

The GOTO-4 telescope (D. Steeghs et al. 2022) is a prototype array of four telescopes with a combined FOV of $\sim$18 $\deg^2$. The GOTO team searched for 29 GW event triggers in LIGO's O3 (B. P. Gompertz et al. 2020), and we include 399 pointings that span the *g* and *V* bands, with a median *g*-band depth of $\sim$19.8 $m_{\rm AB}$.

2.3.4. MMT

The 6.5 m MMT at Fred L. Whipple Observatory in Arizona conducted a galaxy-targeted search with MMTCam for EM counterparts to both GW190425 and S190425c (G. Hosseinzadeh et al. 2019). We include 119 pointings in *g* and *i*, with a median *i*-band depth of 21.9 $m_{\rm AB}$.

2.3.5. Swift

In O3, Swift searched 18 GW events using a galaxy-targeted approach (P. A. Evans et al. 2016), including GW190425, with the Ultra-Violet/Optical Telescope (S. R. Oates et al. 2021). These data include 1357 pointings for GW190425 in the *u* band with a median limiting magnitude of 19.4 $m_{\rm AB}$. These data are particularly interesting as they cover a region of parameter space which is unique given the other optical filters in this combined data set.

2.4. Public Data via Literature Review

2.4.1. Pan-STARRS

The Pan-STARRS data used in this study come from the Pan-STARRS1 (PS1) telescope at the summit of Haleakala on the Hawaiian island of Maui. PS1 is equipped with a composite 1.4 gigapixel camera and has a FOV of 7.06 $\deg^2$ in a circular aperture; this FOV is broken into a tessellation of "'skycells,"[26] each having a dimension of $\sim 24' \times 24'$ (K. C. Chambers et al. 2016). Each skycell can be treated as an individual pointing that inherits the parent's World Coordinate System and image depth, and allows PS1 upper-limits data to be more easily analyzed by Teglon. The PS1 telescope began searching the localization of GW190425 about 80 minutes after the GW trigger, and continued for the following 3 days, publishing their upper limits (S. J. Smartt et al. 2024). The pointings and limits derived from these data were shared with our team via private communication and include 6558 skycells covering a unique sky area of $\sim$1085 $\deg^2$ in the *i* band to an average depth of $\sim$21.5 mag.

2.4.2. ATLAS

The Asteroid Terrestrial-impact Last Alert System (ATLAS) is a network of four identical telescopes, with two telescopes located on the Hawaiian Islands (one on Haleakala and another on Mauna Loa), one telescope in El Sauce, Chile, and the last telescope in Sutherland, South Africa (J. L. Tonry et al. 2018). Each telescope has a rectangular FOV of 28.9 $\deg^2$, and over the course of $\sim$7 days observed the localization of GW190425, publishing their upper limits

[26] https://outerspace.stsci.edu/display/PANSTARRS/PS1+Sky+tessellation+patterns

(S. J. Smartt et al. 2024). The pointings and limits derived from these data were shared with our team via private communication and include 437 pointings covering a unique sky area of $\sim$7110 deg^2 in the ATLAS o and c bands to an average depth of $\sim$18.9 mag.

The combined data for this analysis is shown overplotted the LVK localization contours in Figure 3.

3. Candidates

3.1. 1M2H Vetted Candidates

After subtracting templates from the ANDICAM, Nickel, Swope, and Thacher images, we identified candidate counterparts to GW190425 by searching for sources of positive emission in the difference images. We first ran `DoPHOT` on the difference images, searching for sources detected at a S/N threshold of $\geqslant 3\sigma$. We performed minimal filtering on the detected sources, particularly removing those where >30% of pixels inside the PSF aperture are negative or where >40% of pixels are masked. Apart from these cuts, we required only that a candidate transient is detected in a single image at our S/N threshold.

All candidates were then gathered by field into web pages with cutout images showing the candidate detection from every epoch, the scatter in candidate coordinates for each detection, and the difference light curve in terms of flux and magnitude. Members of the 1M2H collaboration all visually vet these web pages to rule out detections that appear consistent with artifacts such as a convolved cosmic ray, correlated noise across a bad section of each detector, dipole emission associated with a bright and poorly subtracted star, or a satellite or other moving object passing through the image frame.

We required that a candidate transient be flagged only by a single human vetter to elevate that source for our candidate analysis pipeline. Following analysis similar to that of C. D. Kilpatrick et al. (2021a) and public candidates described below, we cross-matched the candidates to sources classified as stars by Gaia (point-source score, PSS > 0.99 following the PSS value from Gaia Collaboration et al. 2021), that were within 2″ of the location of a minor planet at the time of observation based on ephemeris from the Minor Planet Catalog,[27] or were cross-matched to known, public transients in the Transient Name Server (TNS).[28] After these checks, we identified four novel candidate transients that were reported to TNS: AT 2019aasp, 2019aasq, 2019aasr, and 2019aass (D. A. Coulter et al. 2023). These and all other candidate transients reported to TNS were then analyzed using methods described below. In Figure 4, we show photometry from candidates discovered by 1M2H in comparison with model KN light curves described in Section 5.1, and in Figure 5, we show the Swope discovery image of AT 2019aasq, a potential KN we cannot rule out given our vetting process described in Section 3 and Appendix A.1.

3.2. Public Candidates

We used our candidate analysis pipeline to vet candidate counterparts to GW190425 in the context of the final `GW190425_PublicationSamples`[29] localization map, time discovered from merger, coincidence with likely stars or other known point sources and minor planets, spectral classification as a transient type unlikely to be associated with an NS merger, association with a host galaxy outside the localization volume defined by the `bayestar` map, and photometric evolution that does not resemble a likely KN or afterglow counterpart. In general, these cuts follow the methods described by C. D. Kilpatrick et al. (2021a) and the examples implemented by C. D. Kilpatrick (2023). Here we summarize each step.

1. Importation of candidates from our transient database `YSE-PZ` (D. A. Coulter et al. 2023c), which includes all transients and metadata contained in TNS.
2. We analyze only candidates discovered within the first 14 days after the coalescence time of GW190425 on 2019 April 25, 08:18:05 as defined by B. P. Abbott et al. (2020a). Moreover, we only analyze candidates within the 2D 90th percentile as defined by the final `GW190425_PublicationSamples` map of that event. These two initial cuts define our sample of 290 candidate counterparts analyzed in the remaining steps below.
3. We cross-match to minor planets using the time of discovery and coordinates of each candidate and using the Minor Planet Checker.[30] Any source found within 2″ of a known minor planet at the time of observation is ruled out. In total, two candidates were ruled out by this check.
4. We cross-match to point sources within the Gaia (Gaia Collaboration et al. 2021) and Pan-STARRS DR2 catalogs (H. A. Flewelling et al. 2020). For Gaia, this involves checking for sources aligned within 2″ of a source with point-source score >0.99, while for Pan-STARRS we check for candidates within 2″ of a source classified as point-like by the PS1 detection-flagging algorithm.[31] Thirteen candidates were ruled out for coincidence with Gaia sources, while no candidates were ruled out owing to coincidence with Pan-STARRS sources.
5. For candidates with spectroscopic follow-up observations, we rule out those with a spectral classification that is inconsistent with a KN or GRB afterglow. For GW190425, this sample comprises sources classified in TNS as a cataclysmic variable (CV), superluminous supernova (SLSN), SN Ia, SN Ib, SN Ic, SN II, and SN IIn, which are known to arise from progenitor systems other than NS mergers. Thirty-one candidates were ruled out based on their spectral classifications.
6. We rule out candidates with premerger activity within 2″ of the transient location based on a positive detection using forced photometry in ASAS-SN (C. S. Kochanek et al. 2017), ATLAS (J. L. Tonry et al. 2018; K. W. Smith et al. 2020; L. Shingles et al. 2021), or ZTF (E. C. Bellm et al. 2019). For additional details on our querying method, see D. A. Coulter et al. (2023c). We rule out three candidates that have premerger variability.
7. In addition to candidates outside the nominal localization area, we associate all candidates with host galaxies when possible and rule out candidates that are outside the 90th percentile localization volume defined by the final `GW190425_PublicationSamples` localization map.

[27] https://minorplanetcenter.net
[28] https://www.wis-tns.org/
[29] https://gracedb.ligo.org/superevents/S190425z/files/
[30] https://cgi.minorplanetcenter.net/cgi-bin/checkmp.cgi
[31] https://outerspace.stsci.edu/display/PANSTARRS/PS1+Detection+Flags

We derive our host-galaxy sample from those with spectroscopic redshifts in the NASA/IPAC Extragalactic Database (NED)[32] or a photometric redshift from the PS1-STRM (R. Beck et al. 2021), Photometric Redshifts for the Legacy Surveys (Legacy; R. Zhou et al. 2021), or 2MASS Photometric Redshift (2MRS; M. Bilicki et al. 2014) catalogs. Note that we place priors on the galactocentric host offsets of $<300''$ and <75 kpc (consistent with the maximum sGRB host offsets identified by, for example, W. Fong & E. Berger 2013; W.-f. Fong et al. 2022) in selecting the most likely host galaxy, then associate each transient with the galaxy that provides the smallest physical offset from the GW candidate. In this way, we ruled out 183 candidates.

8. Finally, we rule out candidates with photometry whose absolute magnitude, decline rate, or color evolution appears inconsistent with KN or afterglow emission. The details of this calculation are described by C. D. Kilpatrick et al. (2021a). At this stage, there remained 58 viable candidates, of which we ruled out 30 owing to photometric evolution inconsistent with being a counterpart to GW190425. There remain 28 viable candidate counterparts to GW190425 that pass each of the cuts described above and which we consider to be viable counterparts to this event.

Based on each of the steps described above and the lack of spectroscopic follow-up observations, direct characterization of each source as a possible KN or GRB afterglow is difficult, limited to searches for long-lasting emission such as a radio afterglow (e.g., E. Nakar & T. Piran 2011; B. D. Metzger & G. C. Bower 2014). Targeted radio searches of GW190425 did not reveal any promising counterparts, although none of our best candidate counterparts were observed in follow-up radio observations (e.g., by O. M. Boersma et al. 2021). Obtaining spectra of candidate KN and GRB afterglows in the future will require a dedicated framework similar to the above that can ingest and analyze candidate GW counterparts using minor planet, point-source, variability, galaxy, and forced-photometry catalogs in nearly real time. This remains a significant challenge to rapid identification of GW counterparts, as demonstrated by recent follow-up observations of the LVK O4b event S240422ed (A. L. Piro et al. 2024), some of which could have been immediately rejected as viable GW counterparts using available archival data (S. Schulze et al. 2024), thereby conserving follow-up resources. However, in the context of GW190425 and taking the remaining sources in our analysis, we can differentiate between sources that are more likely to be GW counterparts versus interloping transients. We provide a more detailed description of four of the remaining candidates considered to be the most likely counterparts to GW190425 in the Appendix.

4. Teglon

One effective method for localizing the EM counterparts of GW sources is to target the bright/massive galaxies residing in the locus of high probability within a GW localization volume (J. Kanner et al. 2012; N. Gehrels et al. 2016). This technique relies on two key factors: a galaxy catalog that is relatively complete at the ranges where GW sources are likely to be detected, and localization regions that are small enough to be efficiently searched with ground-based telescopes. To date, several catalogs have been used in GW follow-up searches (R. K. Kopparapu et al. 2008; D. J. White et al. 2011; G. Dálya et al. 2018, 2022; D. O. Cook et al. 2023), and all contain the key attributes of position, distance, and B-band magnitudes. The B band is used in particular because the rate of BNS mergers is expected to follow the star formation rate (SFR) in the local Universe, and B is a convolution of this SFR with a galaxy's total stellar mass (E. S. Phinney 1991; K. Belczynski et al. 2002). In 2017, this technique led to the discovery of the first optical counterpart, AT 2017gfo (D. A. Coulter et al. 2017), to a GW source, GW170817. GW170817 was the first ever BNS merger detected in GWs, and localized to an area of 31 deg^2 and a luminosity distance of 40^{+8}_{-14} Mpc (B. P. Abbott et al. 2017d). In searching for this counterpart, 1M2H used the Gravitational Wave Galaxy Catalogue, which at 40 Mpc is nearly 100% complete when compared to a Schechter galaxy luminosity function (P. Schechter 1976) for galaxies with a characteristic luminosity of $\leqslant -20.3$ mag.

However, as the LVK has improved the GW network detection sensitivity (B. P. Abbott et al. 2016c), these catalogs and techniques have become less effective. In O3, the typical BNS inspiral range was ∼108–135 Mpc (R. Abbott et al. 2021). For BNS mergers $>2.8\,M_{\odot}$, or face-on mergers, the detection distance may be much larger. As BNS detection ranges increase, the surface density of galaxies in projection increases so that any FOV should contain many galaxies (both cataloged and uncataloged). Naively, a pure tiling approach to searching for a counterpart is more effective at larger distances, but this picture is complicated by inhomogeneous galaxy catalog coverage. Intelligently trading off between these two approaches—to use our knowledge of where galaxies are to target them and to tile the localization region when we do not—motivates the creation of a new tool called `Teglon`. A detailed treatment of how `Teglon` transforms GLADE, implements its completeness weighting, and calculates its pixel-level upper limits will be presented in a forthcoming companion paper.

4.1. GW190425 Transformed By `Teglon`

`Teglon`'s EM search optimization depends on two properties: the B-band luminosity completeness of its volume pixels (or voxels) in the GW localization volume, and how much area that GW localization volume subtends on the sky in projection. Completeness is largely dictated by the average luminosity distance to an event; however, in regions of high galaxy catalog completeness such as SDSS Stripe 82 (J. Annis et al. 2014) or the survey footprint of 2dF (M. Colless et al. 2001), `Teglon`'s algorithm can still be effective at redistributing probability in the original GW localization to high-probability galaxies, thereby reducing the area an instrument needs to search. However, the area in projection of a GW localization also matters: If the area subtended by a GW localization fits within the FOV of a search instrument (e.g., GW170817's localization), redistributing probability on scales smaller than the FOV would not change the search strategy. In the edge case of 0% completeness, or very small projected areas, `Teglon`'s optimization is identical to a pure tiling pattern of the high-probability region.

The localization of GW190425 is a quintessential use case for `Teglon`. Because this event was only detected by the LIGO Livingston detector, its location was constrained to nearly a quarter of the sky (9881 deg^2). However, despite this

[32] http://ned.ipac.caltech.edu/

Table 1
1M2H UVOIR Imaging of the GW190425 Localization Region

Source[a]	α (J2000)	δ (J2000)	Exposure Time (s)	Date[b] (MJD)	Filter	Magnitude Limit[c] (3σ)
ANDICAM CCD	17:31:09.72	−08:27:14.40	900	58599.2453	*I*	21.60
ANDICAM CCD	16:52:07.06	−17:03:27.72	240	58599.2798	*I*	19.91
…	…	…	…	…	…	…
ANDICAM IR	17:31:10.54	−08:26:56.04	30	58599.2012	*K*	14.28
ANDICAM IR	16:52:07.90	−17:03:09.36	30	58599.2797	*H*	14.27
…	…	…	…	…	…	…
Nickel	13:54:45.17	+44:46:44.76	600	58599.1986	*r*	21.09
Nickel	13:54:45.22	+44:46:44.40	600	58599.2059	*i*	20.44
…	…	…	…	…	…	…
Swope	05:48:48.14	−25:21:50.04	180	58598.9937	*i*	21.01
Swope	16:48:15.84	−17:25:10.56	180	58599.1293	*i*	20.84
…	…	…	…	…	…	…
Thacher	11:59:16.61	+21:05:57.48	180	58599.2363	*r*	18.50
Thacher	12:08:15.62	+25:15:54.72	180	58599.2414	*r*	17.93
…	…	…	…	…	…	…

Notes. We only include data that 1M2H acquired and reduced. For LCO data, referred to in Section 2, these data are published in I. Keinan & I. Arcavi 2025. For all other data, see the curated pointings on the Treasure Map (S. D. Wyatt et al. 2020).
[a] Imaging as described in Section 2.
[b] MJD is taken from the center of the exposure time.
[c] In-band 3σ limit for the reported image as described in Sections 2 and 5. All magnitudes are on the AB system (J. B. Oke & J. E. Gunn 1983).
(This table is available in its entirety in machine-readable form in the online article.)

large area, the distance was relatively close, at 159 Mpc (B. P. Abbott et al. 2020a). At this distance, the GLADE catalog is on average ∼50% complete, and therefore `Teglon` redistributed half of the localization probability to galaxies at the correct distance. This redistribution reduces the 90th percentile localization to 6674 deg^2, a factor of ∼1.5, and also changes the relative weight of each underlying map pixel—changing the relative probability covered by each reported observation in the full data set. Figure 6 shows the resulting localization, with insets that highlight this updated concentration of probability.

In the context of the EM search for a counterpart, Table 2 shows a synoptic view of the effect `Teglon` has on the search efficiency increase, η, for each instrument in the data set. The value of η is markedly enhanced for detectors with FOV $\leqslant$1 deg^2. In general, these instruments followed a galaxy-targeted approach, and owing to the moderate completeness of GLADE with respect to GW190425's localization, the redistributed map provided by `Teglon` confirmed that these galaxies were in regions of the sky more likely to host the progenitor of the GW event. For this particular event, 3402 of the original map pixels (∼178 deg^2) had their probability values boosted by factors of $\geqslant$10 over their original values, and constitute 16% of the total probability in the map.

For this data set, while all instruments have $\eta \geqslant 1.0$, instruments with FOV $\geqslant$1 deg^2 saw diminishing returns owing to the fact that their large footprint on the sky allowed them to simply tile the entire Western Spur of the localization (see Figure 3). Because of this, the survey footprint of these instruments encompassed both the pixels where probability was being concentrated and the voids left in between, resulting in η approaching unity. However, in the maximal case where a GW event subtends the entire sky but is detected at a distance where GLADE is 100% complete (e.g., at the distance of GW170817, 40 Mpc), `Teglon` would be useful for even the largest FOV instruments.

After an EM search has concluded, `Teglon` can also be used to calculate the detection efficiency on any arbitrary model with light curves generated within the passbands of the covering observations. Our new algorithm operates on the pixel level, combining the line-of-sight extinction, covering-observation limiting magnitude, LVK GW distance prior, and `Teglon`-redistributed GW probability on a per-pixel basis. The particulars of this calculation are described in detail in Appendix A.2.

5. Model Comparisons

Based on the results of Section 3.2, we do not consider any of the 28 remaining EM transients from our analysis as likely counterparts to GW190425, and interpret the image depth for the data presented in Table 1 and in the TM (described in Section 2) as limits on a few classes of hypothetical EM counterparts to a BNS merger. To make this physically meaningful, we assume (and in the case of the data in Table 1, we know) that the data are homogeneous in that (1) each datum is the result of subtracting an in-band template image from the search image using the same instrument configuration, and (2) the reported depth of each image was computed by estimating the $\geqslant 3\sigma$ limiting magnitude from the difference image. We perform the joint model detection efficiency calculation, combining all reported epochs, depths, and filters, using the formalism described in Appendix A.2. The maximum probability to detect any model is limited by the total amount of probability that the full data set covers; therefore, we report our detection probability in two ways: (1) as the probability calculated by Equation (A4), and (2) as a percent of the total amount of redistributed probability reported in Table 2, 48.28%, i.e., X% (X/48.28%). This relative detection efficiency characterizes the effectiveness of the observations themselves, assuming they could have covered the entire localization region.

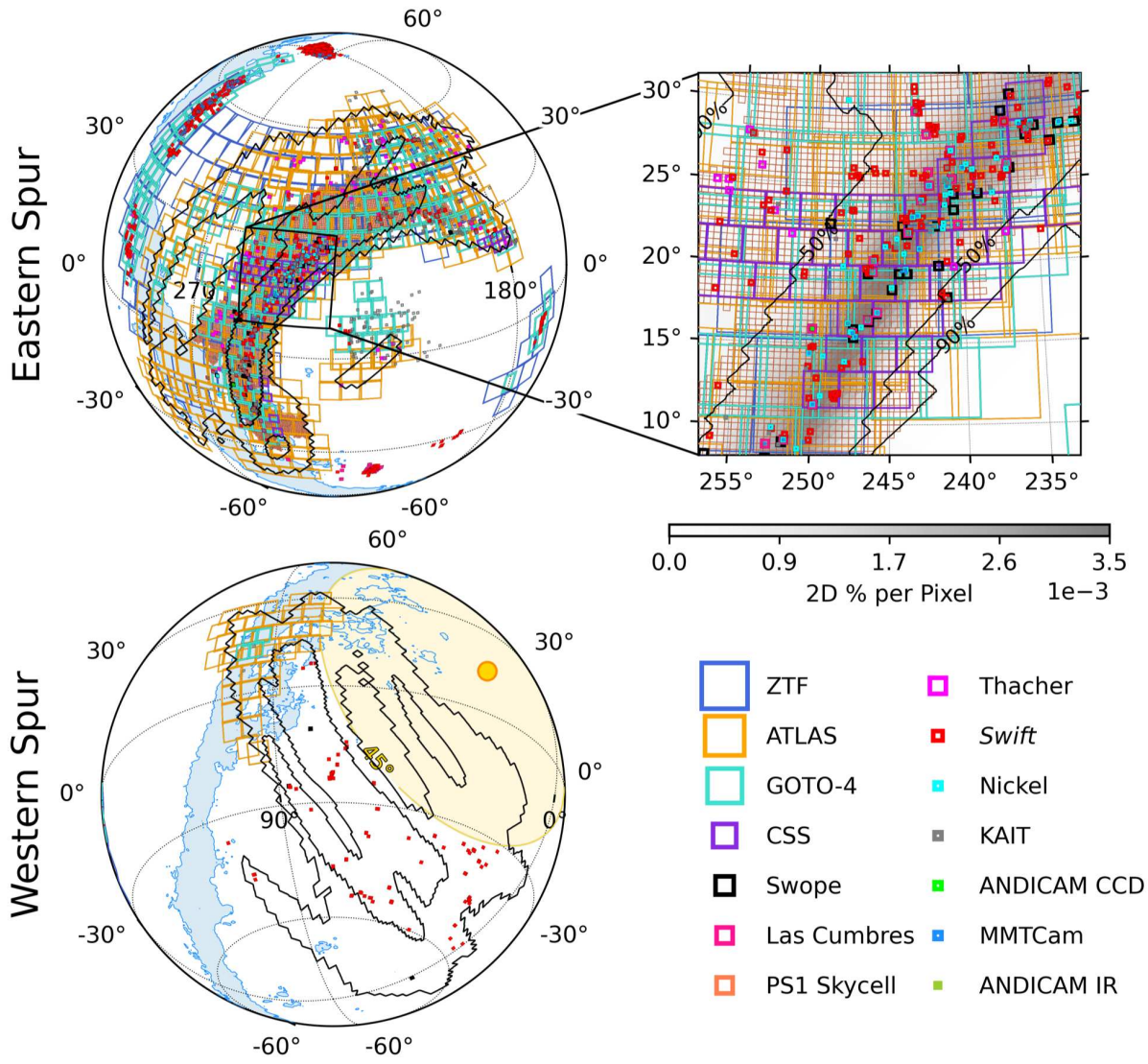

Figure 3. Visualization of the full EM search data set for this work. In each orthographic projection, black contours correspond to the 50th/90th localization of GW190425, and Milky Way extinction is marked as a blue contour at $A_r = 0.5$ mag. Overplotted are all instrument FOVs: ZTF (dark blue), ATLAS (light orange), GOTO-4 (turquoise), CSS (purple), Swope (black), Las Cumbres (magenta), PS1 Skycells (dark orange), Thacher (hot pink), Swift (red), Nickel (cyan), KAIT (gray), ANDICAM CCD (lime green), MMTCam (light blue), and ANDICAM IR (dark green). Upper left: close-up view of the Eastern Spur of probability as seen in Figure 1, R.A. ∈[95, 315] degree. Every instrument in our manifest has imaging in this hemisphere (10,365 total field centers; 266 not shown), covering 45.2% of the final LVK 2D probability. Upper right: a 12° radius zoom in on R.A. 245°, decl. +20°, showing a detailed view of the smaller FOV instruments. The grayscale gradient is the 2D probability of the localization, with the 50th/90th contours labeled. Many of these fields covered the same sky regions multiple times in the same filters and highlight an opportunity to coordinate EM follow-up efforts (see Section 6), with similar candidate identifications reported (e.g., by M. W. Coughlin et al. 2019; M. J. Lundquist et al. 2019). Lower left: close-up view of the Western Spur of probability as seen in Figure 1, R.A. ∈[0, 95] degree. Only ATLAS, GOTO-4, Swope, and Swift have observations in this hemisphere (355 total) owing to this region being close to the Sun, contributing only 3.1% of the covered 2D probability. A yellow Sun contour denotes a 45° separation that marks Swift's pointing limits.

5.1. Kilonovae

The discovery of the EM counterpart to GW170817, the KN AT 2017gfo (B. P. Abbott et al. 2016d; D. A. Coulter et al. 2017), demonstrated that BNS mergers are associated with short-lived thermal transients with luminous UVOIR emission, consistent with radioactive decay of freshly synthesized heavy elements (M. R. Drout et al. 2017). Surprisingly, observations of AT 2017gfo showed that multiple ejecta components of different compositions (i.e., opacities) were required to accurately model its light curves (P. S. Cowperthwaite et al. 2017; C. D. Kilpatrick et al. 2017; V. A. Villar et al. 2017).

Motivated by this finding, we consider two fiducial KN models, a "blue" KN and a "red" KN, following the prescription of V. A. Villar et al. (2017) to generate models with varying ejecta masses ($M_{\rm ej}$), velocities ($v_{\rm ej}$), and opacities (see also V. A. Villar et al. 2017). We do so in the Modular Open Source Fitter for Transients (`MOSFiT`) framework (J. Guillochon et al. 2018), with fixed parameters and bandpasses matched to our data set. We adopt $\kappa = 0.5$ cm^2 g^{-1} as the "blue" model and $\kappa = 3.65$ cm^2 g^{-1} as the "red" model, matching the parameters for a two-component model originally presented by P. S. Cowperthwaite et al. (2017) and V. A. Villar et al. (2017). Furthermore, in the context of an extremely lanthanide-rich model with high opacities, we

Table 2
GW190425 Search Synopsis

Search Instrument	FOV (deg^2)	No. of Fields	Total 2D Probability $\sum_i P_{2D_i}(\%)$	Total Redistributed Probability[a] $\sum_i P''_{2D_i}(\%)$	Efficiency Increase $\eta \equiv \sum_i \frac{P''_{2D_i}}{P_{2D_i}}$
ANDICAM IR	0.0015	21	0.04	0.46	11.36
MMTCam	0.0020	118	0.15	1	6.44
ANDICAM CCD	0.0112	27	0.06	0.62	10.39
KAIT	0.0128	412	0.23	1.7	7.37
Nickel	0.0438	137	0.19	0.92	4.98
Swift	0.0803	1357	0.72	3.84	5.32
Thacher	0.1200	186	0.09	0.42	4.54
Las Cumbres	0.1951	754	0.35	1.42	4.02
Swope	0.2459	204	0.59	1.87	3.19
CSS	4.9997	61	6.15	6.98	1.13
PS1[b]	7.068	148	18.79	19.99	1.06
GOTO-4	18.1300	399	30.48	32.01	1.05
ATLAS	28.8906	437	47.02	45.84	0.97
ZTF	46.7253	313	28.99	30.4	1.05
All tiles	9078.59[c]	10,984	48.13	48.28	1.00[d]

Notes. A synopsis of `Teglon`'s effect on the community's combined EM search campaign for GW190425. `Teglon` strongly enhances η for instruments with FOV $\leqslant$1.0 deg^2; see Section 4.1.
[a] See Section 4 for a detailed description.
[b] The Pan-STARRS1 (PS1) effective FOV is calculated from the average number of PS1 skycells in a fiducial PS1 FOV.
[c] Total unique area covered by all observations.
[d] Efficiency boost approaches 1 as both more area is observed and the FOV of the instrument increases; however, this relation is not monotonic because it depends on whether the original pointings remain in high-probability locales after `Teglon` redistributes probability.

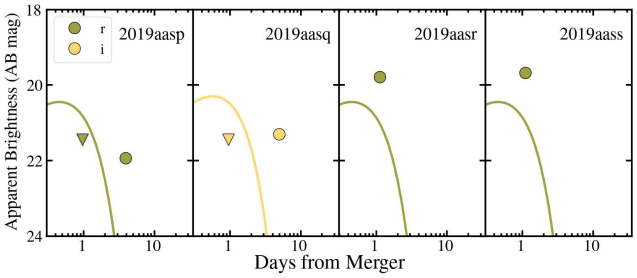

Figure 4. Photometry of the four transients discovered within the localization region of GW190425 by 1M2H and described in Section 3.1. We show the time of detection as a circle in each panel, with green corresponding to *r*-band photometry and yellow to *i*-band photometry. Downward arrows correspond to upper limits. For comparison, we overplot model KN light curves for a hypothetical event with ejecta mass 0.023 $M_\odot$, velocity 0.26*c*, and an electron fraction $Y_e = 0.45$ as described in Section 5.1. As shown in Table 3, we are able to rule out AT 2019aasp as being associated with GW190425 for association with a Gaia star, AT 2019aasq for its apparent rise in brightness based on our *i*-band photometry, and AT 2019aasr for premerger detections (see discussion of our rejection criteria in Section 3.2).

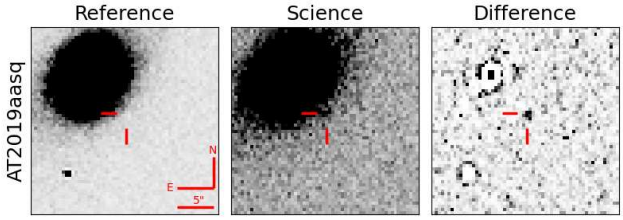

Figure 5. Image cutout triplet for AT 2019aasq, a counterpart candidate discovered by the Swope telescope +4.93 days after the GW trigger that our analysis cannot rule out as a candidate counterpart to GW190425 and which we characterize as a "more likely" KN candidate (see Sections 3 and Appendix A.1 for a detailed discussion). Both the reference (left; MJD 58638.18288) and science (middle; MJD 58603.27694) images were obtained by Swope and show the same 26.″1 × 26.″1 region of sky centered on AT 2019aasq. The difference image (right) highlights the discovery detection of the transient at $i = 21.30 \pm 0.19$ mag. We note that the candidate is clearly visible ∼7.″5 from the center of its likely host galaxy WISEA J154032.14 +282013.7 at $z = 0.031090$ (D. A. Coulter et al. 2023), within the 1σ most likely GW190425 volume. AT 2019aasq was not detected with either ATLAS *c* or *o* bands or ZTF *g* or *r* bands, despite coverage within days of this detection, implying it was likely an intrinsically red, faint transient.

consider $\kappa = 10\,cm^2\ g^{-1}$, which is also the highest-opacity model adopted by V. A. Villar et al. (2017). Otherwise, we consider ejecta masses of 0.001–0.5 $M_\odot$ and velocities of 0.05*c*–0.50*c* for all sets of models. Finally, these models are characterized by a "freeze out" temperature, which sets the minimum temperature reached by the blackbody KN spectrum. We set this value to 2500 K following findings for AT 2017gfo by M. R. Drout et al. (2017). For each KN model set, we show our estimated detection probabilities in Figure 7. We detect a blue, AT 2017gfo-like KN at 28.4% (59.0% relative to the total coverage) and are insensitive to a red, AT 2017gfo-like KN at 2.9% (6.0%). Similarly, in Figure 8 we show that we are also largely insensitive to detecting two additional realizations of even higher-opacity red models ($\kappa = 10.0\,cm^2\ g^{-1}$) expected from a high-mass BNS or NSBH mergers. From these constraints, an immediate conclusion is that to be sensitive to more massive events (e.g., another GW190425-like or NSBH event), EM teams should search at redder wavelengths with deeper limits.

Similar analyses were conducted in the literature, but using different assumptions about the limiting magnitude of each survey, the precise coverage of the GW190425 volume (e.g., not using our redistribution algorithm), and comparison to AT 2017gfo-like KN models as a function of time. The

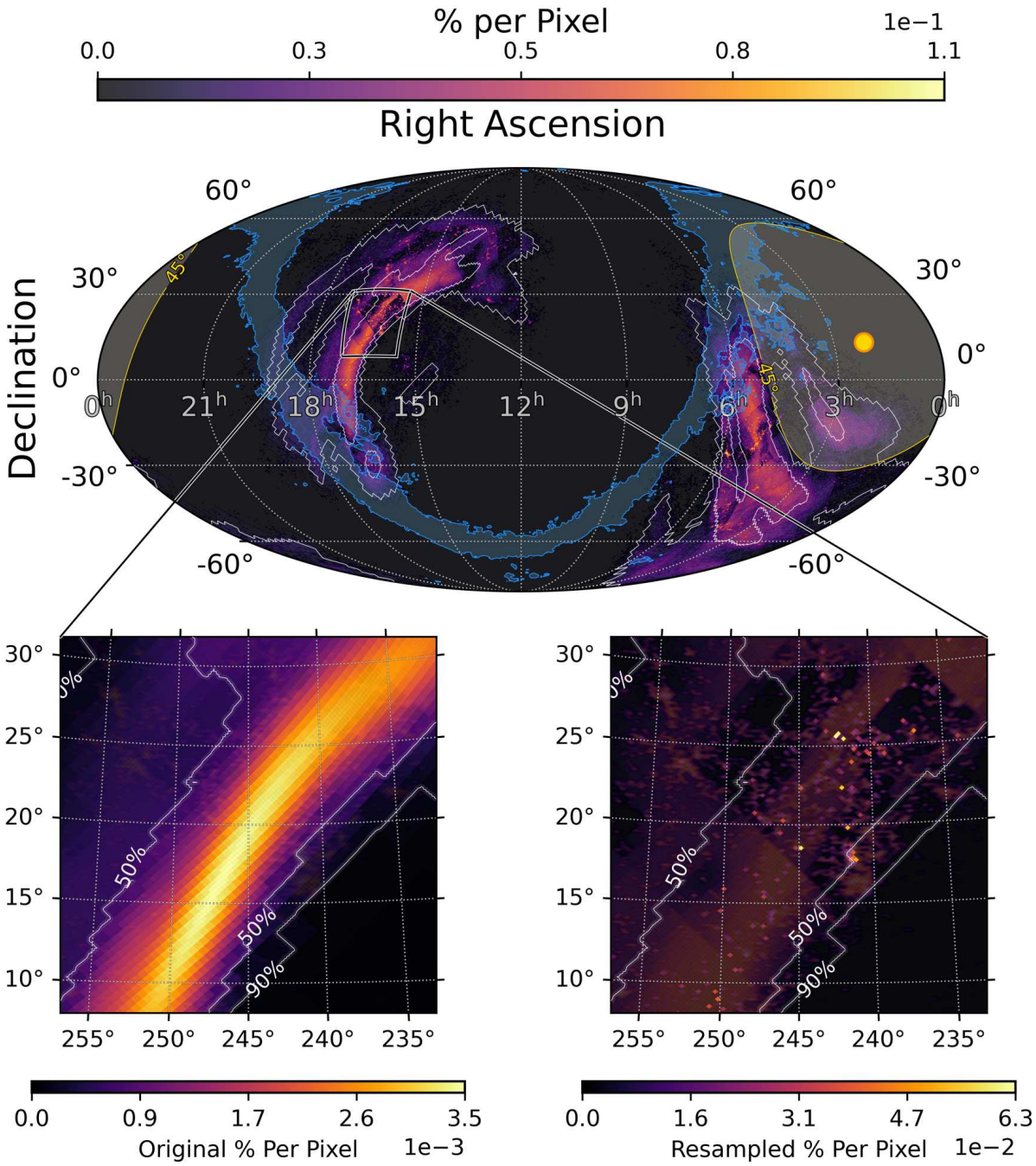

Figure 6. Top: the localization map resampled by `Teglon`. At GW190425's distance, `Teglon` redistributes half of the total 2D probability to the highest-probability galaxies (see Section 4.1). A 12° radius zoom-in panel is marked by a square centered on R.A. 245°, decl. +20°. All other attributes are the same as in Figure 1. Bottom left: for comparison, we show a zoom in of the original localization map, with white contours denoting the original 50th/90th localization. Within the bounding box of R.A. ∈[235, 255] degree and decl. ∈[1030] degree, there is ∼8.2% of the localization probability within ∼377 deg^2. Bottom right: the same zoom-in region with `Teglon`'s redistribution algorithm (matching the top plot). The same amount of probability (∼8.2%) is covered in only ∼100 deg^2, increasing the coverage efficiency by a factor of ∼3.8.

most direct comparison we can make is between our AT 2017gfo-like "blue" KN and values reported in each of these publications. M. W. Coughlin et al. (2019) report that they cover ∼46% of the GW sky map with ZTF to a depth of 21 mag in the *g* and *r* bands, M. J. Lundquist et al. (2019) have coverage of 3.0% to ∼21.3 mag in the CSS open band, S. Antier et al. (2020) achieve 2.8% coverage by the GRANDMA network to 17–23 mag, G. S. H. Paek et al. (2024) report 32.3% coverage to ∼19–22 mag, and S. J. Smartt et al. (2024) obtain 24.9% coverage to 21.3 mag depth in the *i* band, providing an upper limit on their efficiency of detecting an AT 2017gfo-like KN. Similarly, G. Hosseinzadeh et al. (2019) report an AT 2017gfo-like KN detection efficiency of 1.5%, B. P. Gompertz et al. (2020) have 8.1%, and R. L. Becerra et al. (2021) find 2%. These limits are consistent with our cumulative analysis of a 28.4% detection efficiency, which combine most of the reported depths into a single joint analysis.

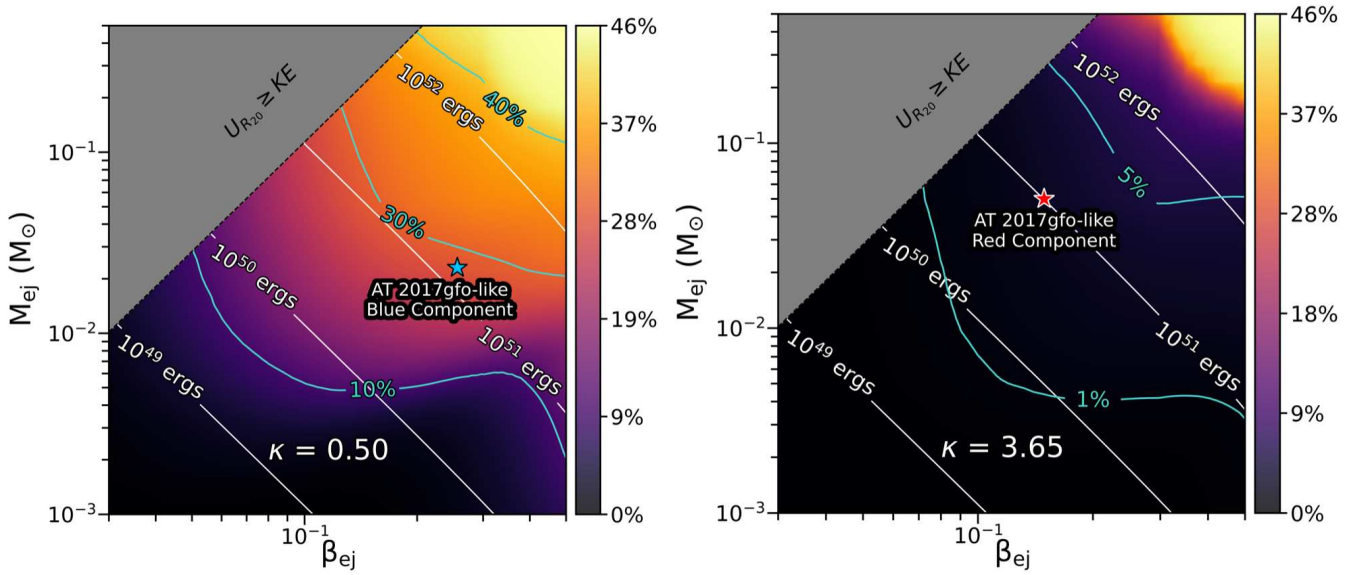

Figure 7. Detection probabilities for KN models from V. A. Villar et al. (2017) as a function of ejecta mass (M_{ej}, in solar masses), ejecta velocity (β_{ej}, in natural units), and opacity (κ). In the upper-left corner of each plot, we have grayed out the region where the binding energy of the ejecta mass exceeds its kinetic energy assuming a stiff NS equation of state and an NS radius of 20 km. We show contours of equal probability in turquoise and contours of equal kinetic energy for the ejecta in white. Model values for AT 2017gfo-like components are taken from Table 2 of V. A. Villar et al. (2017). Left: KN models with $\kappa = 0.50$ cm^2 g^{-1}, overplotted with the blue component of AT 2017gfo ($\beta_{ej} = 0.256$, $M_{ej} = 0.023\,M_\odot$), which we can rule out at a detection probability of 28.4%. Right: KN models with $\kappa = 3.65$ cm^2 g^{-1}, overplotted with the red component of AT 2017gfo ($\beta_{ej} = 0.149$, $M_{ej} = 0.050\,M_\odot$), which we cannot rule out at a detection probability of 2.9%.

5.2. sGRB

We adopt an sGRB afterglow model, `JetFit`, originally presented by Y. Wu & A. MacFadyen (2018) and Y. Wu & A. MacFadyen (2019), and used to model the afterglow light curve of GRB 170817A in the literature (e.g., A. Hajela et al. 2019, 2022; C. D. Kilpatrick et al. 2022). For our fiducial model, we adopt the general parameters from the best fit to the multiwavelength GRB 170817A light curve of A. Hajela et al. (2022). These fixed parameters correspond to the electron energy fraction $\log \epsilon_e = -1$, the magnetic energy fraction $\log \epsilon_B = -5.17$, the spectral index of the electron distribution $p = 2.15$, the asymptotic Lorentz factor $\eta_0 = 8.02$, and the boost Lorentz factor $\gamma_B = 12$. We then vary the explosion energy E_0, the ambient density n, and the viewing angle θ_{obs} to generate in-band light curves from our fiducial model. We consider a range of ambient densities in units of particles per cm^3, n $\in [10^{-6}, 10]$ cm^{-3}, and isotropic equivalent energy $E_{k,iso} = 2E_0/(1 - \cos(1/(2\gamma_B))$ in units of 10^{51} erg (foe), $E_{k,iso} \in [10^{-3}, 100]$ foe, consistent with observed sGRB afterglows in W. Fong et al. (2015). Finally, we considered two viewing angles ($\theta_{obs} = 0$ and $\theta_{obs} = 17°$) for an "on-axis" and "off-axis" model (respectively), but report only on our relatively insensitive on-axis limits because our off-axis models are substantially fainter. In Figure 9 we show that our resulting model detection probability for an on-axis GRB 170817A-like model is 0.40% (0.83%).

5.3. Generic Models

KN and sGRB afterglows have extremely short rise times, and it is likely that ground-based discoveries catch only their decline (I. Arcavi et al. 2017a; M. R. Drout et al. 2017; C. D. Kilpatrick et al. 2017). Motivated by this, we include a generic class of empirical models parameterized by a peak absolute magnitude at the time of the merger, M_0, and a linear decline rate, ΔM, in units of mag day^{-1}:

$$M(t) = M_0 - \Delta M\,(t - t_0)\,, \quad (1)$$

where t is in days. We make these models agnostic in their emission mechanism and construct their light curves with a flat spectral energy distribution (SED). As most of our limits are in the optical range, we emphasize that this implies our constraints are mostly relevant to generic optical transients. Models are considered that span a peak magnitude range $M_0 \in [-14, -20]$ mag and decline rates of $\Delta M \in [10^{-3}, 1.5]$ mag day^{-1} (in log space) to cover a parameter range that includes AT 2017gfo and several classes of well-known transients.

In Figure 10, we show our results, with parameters for AT 2017gfo representing an average of its decline across blue and red bands ($M \approx -16$ mag; $\Delta M \approx 0.7$ mag day^{-1}) and a collection of transient types overplotted in juxtaposition (referenced from M. R. Siebert et al. 2017) and optical emission from sGRBs (the earliest r-, R-, and I-band constraints for GRBs with two detections in the same band from J. C. Rastinejad et al. 2021, and references therein). To the limits of this data set's coverage, we confidently detect these well-known extragalactic transient types, reinforcing the results reported in Section 3. We rule out an AT 2017gfo-like model at 39.3% (81.4%) confidence.

6. Discussion

As the second BNS merger identified by the LVK, GW190425 had significantly different source properties from the first BNS event GW170817. In particular, the much larger total system mass of $3.4^{+0.3}_{-0.1}\,M_\odot$ compared with $2.73^{+0.04}_{-0.01}\,M_\odot$ (B. P. Abbott et al. 2017d) may lead to a significantly different EM counterpart (see R. J. Foley et al. 2020). Now that the LVK's O4 run is well underway, we are faced with a new paradigm for EM searches: more distant events owing to an

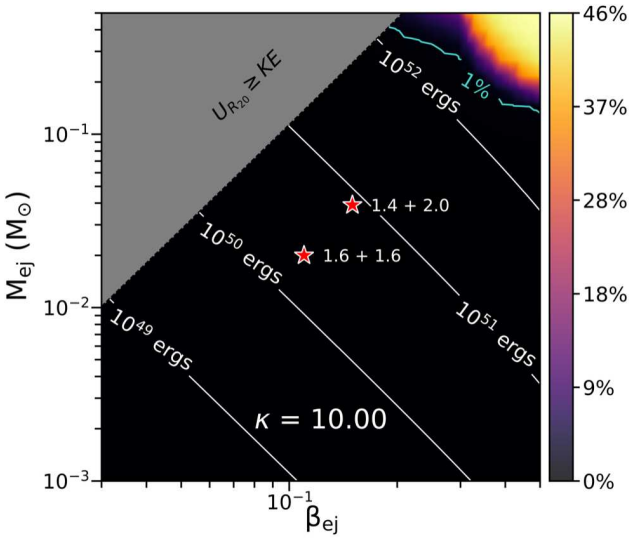

Figure 8. Similar to Figure 7 for "red" KN models in the same style as Figure 7, with $\kappa = 10.0$ cm^2 g^{-1}, chosen to reflect the high opacity of neutron-rich ejecta expected from a BNS merger that directly collapses to a BH. Overplotted are two realizations of ejecta mass and ejecta velocity of speculative KNe, following the arguments of R. J. Foley et al. (2020), based on models from S. Rosswog et al. (2013), that consider the case where the merging NSs have equal mass ($1.6\,M_\odot + 1.6\,M_\odot$) or if one NS was more massive ($1.4\,M_\odot + 2.0\,M_\odot$). We cannot rule out these red models given the depth of this combined data set.

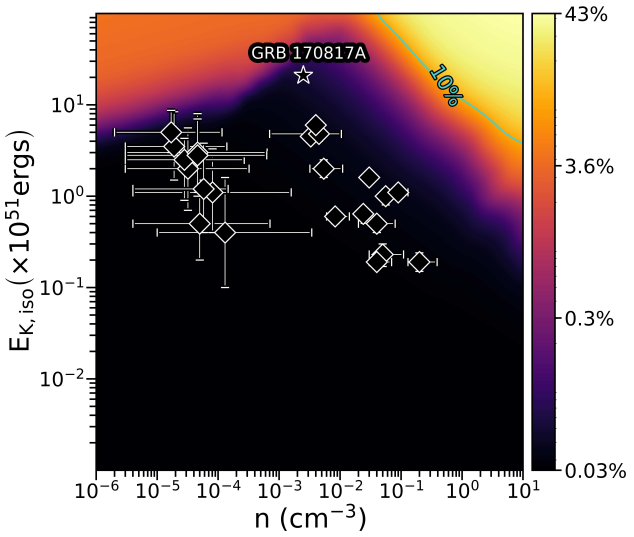

Figure 9. Similar to Figure 7 for on-axis ($\theta_{obs} = 0°$) sGRB models from Y. Wu & A. MacFadyen (2018) as a function of isotropic kinetic energy $E_{k,iso}$ and circumburst density n. For reference, we note the location of a GRB 20170817A-like afterglow with $E_{k,iso} = 2.1 \times 10^{52}$ erg and $n = 2.5 \times 10^{-3}$ cm^{-3} from A. Hajela et al. (2019), which is broadly consistent with multiwavelength modeling of that burst from G. P. Lamb et al. (2019) and E. Troja et al. (2020). The area of relatively high detection probability at low densities and high energies is owing to elevated optical brightness in the model on extremely short timescales contemporaneous with serendipitous ZTF imaging. This phenomenon arises when the peak timescale of the GRB afterglow is long for on-axis afterglows due to low circumburst density, which increases $t_{peak} \propto (E_{k,iso}/n_0)^{1/3} \times \theta_j^{5/2}$ (see, e.g., E. Troja et al. 2017; Y. Wu & A. MacFadyen 2018).

increase in detector sensitivity, larger than expected localization areas caused by Virgo's unexpected downtime during O4a, and an intrinsic diversity in BNS and NSBH systems leading to a range of EM counterparts. Therefore, it is likely that the search strategies that worked for GW170817 will have to be updated. To address these scenarios in O4 and beyond, we consider several updates to `Teglon` which will enhance existing capabilities and add new ones. Here we explore our plan to optimize a network of telescopes engaged in a counterpart search, add new catalogs to `Teglon` to enable new types of counterpart searches, and consider combining different types of localization information and source properties from coincident sources such as fast radio bursts (FRBs), GRBs, and neutrino detections into `Teglon`.

6.1. EM Follow-up Coordination

If we sum the product of every pixel with the multiplicity of observations that cover it and divide that number by 2—one epoch for a search image and one epoch for a template image—the total area of observations we analyze in Section 4 could have uniquely covered ∼17,735 deg^2, or roughly 1.8 times the final 90th percentile localization region, ignoring considerations for observing site, timing, and observability on the sky. This ratio between the total area surveyed and 90th percentile localization region is even larger if we only consider the portions of the sky with no Sun constraint (i.e., the Eastern Spur of probability; see Figure 3). However, the EM community's follow-up strategy for GW sources is uncoordinated between observational teams, as evidenced by the search statistics shown in Table 2—only 5638 deg^2 of localization area was uniquely searched. Furthermore, as seen in Figure 3, ZTF covered nearly the entire Eastern Spur of probability in g and r over the course of the first 3 nights. Despite this, there were ∼900 other images taken of these same fields in the same filters within the same time period with five other instruments. In our analysis, these additional images offer little constraining power on the models that we consider. Despite the stroke of luck of GW170817 merging at a distance of only 40 Mpc, and its counterpart AT 2017gfo being discovered just ∼11 hr later, no KN was localized in O3 and the prospects for localizing one in O4 remain challenging. Increasing the coordination between follow-up facilities can drastically increase the odds of rapidly and precisely localizing the next KN by leveraging `Teglon` to design strategies that can optimize our sensitivity to a range of counterpart models.

To address these challenges, in an upcoming enhancement `Teglon` will publish its redistributed localization map as a dynamic, real-time service that can be subscribed to by a network of telescopes. Combined with real-time observation reporting systems such as the GW TM (S. D. Wyatt et al. 2020) for individual GW events, any telescope can take advantage of `Teglon` queries for the next best observation not currently covered by another facility. When an observation is scheduled, `Teglon` will decrement the probability in the pixels that are covered, and the following query for the next best observation will be dynamically updated. This coordination function will operate on a per-filter basis, allowing different passbands to be optimized independently. Finally, the pixel probability decrementation will be dynamic: `Teglon` will alter the probability proportional to a model-specific light curve as a function of filter. For instance, while KNe quickly decline in blue bands, they rise more slowly in red bands. For joint searches in blue and red filters, `Teglon` will restore probability to covered pixels at different rates to force successive observations back to regions of high 2D probability

depending on what filter the search instrument is using. In this way, Teglon will optimize a network of search telescopes in both their spatial coverage and model sensitivity. Teglon's underlying galaxy catalog can also be easily updated, for example by replacing GLADE with the NED Local Volume Sample (NED-LVS; D. O. Cook et al. 2023), leveraging both the NED-LVS's higher completeness beyond ∼80 Mpc and its derived physical properties (e.g., SFR and stellar mass) for a new galaxy prioritization algorithm.

6.2. FRB 190425A and Combining Coincident Sources within Teglon

While no optical counterparts were discovered in our follow-up campaign or imaging from other efforts that appear consistent with a KN or GRB afterglow from GW190425 (M. W. Coughlin et al. 2019; G. Hosseinzadeh et al. 2019; M. J. Lundquist et al. 2019; S. Antier et al. 2020; B. P. Gompertz et al. 2020; R. L. Becerra et al. 2021; G. S. H. Paek et al. 2024; S. J. Smartt et al. 2024),[33] A. Moroianu et al. (2023) reported the potential coincidence between FRB 190425A and GW190425 based on the former's detection inside the 90th percentile credible region of the latter and discovery of the FRB 2.5 hr after the GW190425 merger. Given their highly energetic radio bursts, millisecond timescales, and the discovery of an FRB from the Galactic magnetar SGR J1935+2154 (C. D. Bochenek et al. 2020; CHIME/FRB Collaboration et al. 2020; B. Zhang 2023), FRBs are thought to arise from or in the immediate environments of magnetars (see, e.g., B. Margalit et al. 2019; B. D. Metzger et al. 2019; M. Lyutikov et al. 2020, for a discussion of various FRB emission models involving magnetars). Invoking the formation of a magnetar in the postmerger collapse of a BNS system (B. Zhang 2013; E. R. Most et al. 2018), FRBs may be credible radio counterparts to BNS mergers, and combining observables from GW events and FRBs within Teglon can aid in rapid localization and identification of likely host galaxies (similar to the analysis of FRB 20190425A by F. H. Panther et al. 2023).

Given the hard-X-ray detection of SGR J1935+2154 contemporaneous with its FRB (S. Mereghetti et al. 2020; C. K. Li et al. 2021; A. Ridnaia et al. 2021), near-contemporaneous constraints on a fast optical burst or afterglow can provide a novel way of localizing GW counterparts (e.g., on milliseconds to hours timescales, as by I. Andreoni et al. 2020; C. D. Kilpatrick et al. 2021b, 2024). As a test case, we analyzed all of our candidates and imaging in the context of FRB 20190425A. None of the optical transients we analyze or 1M2H imaging uniquely reported here fall within the localization of the FRB, leaving the PS1, ATLAS, and ZTF limits on afterglow-like emission from a hypothetical magnetar that were analyzed by S. J. Smartt et al. (2024). These limits constrain the presence of an optical counterpart to ∼21 mag on timescales of hours, which is detectable via a nonthermal afterglow in the plasma around a magnetar assuming an extremely energetic magnetar burst ($>10^{47}$ erg) or a dense medium ($>10^4$ cm^{-3}) following optical predictions from B. D. Metzger et al. (2019) and C. D. Kilpatrick et al. (2021a).

While arcsecond-scale localization of FRBs is possible with interferometers such as ASKAP (J.-P. Macquart et al. 2010), the Very Large Array (C. J. Law et al. 2018), MeerKAT (K. M. Rajwade et al. 2022), and now the CHIME Outrigger sites (S. Andrew & Chime/FRB Collaboration 2025), the vast majority of known FRBs have been discovered with localizations of several deg^2 (including FRB 20190425A by CHIME; CHIME/FRB Collaboration et al. 2021). At these angular scales, the Teglon algorithm is effective at selecting high-likelihood galaxies within the 2D localizations of both maps, for example by assuming that both the 2D localization provided by the LVK ($P_{\rm 2D,GW}$) and the CHIME beam ($P_{\rm 2D,FRB}$) represent independent estimates of the same source location and are combined into a single map ($P_{\rm 2D_k} = P_{\rm 2D,GW} \times P_{\rm 2D,FRB}$). This assumption can be extended to any class of sources with localization on angular scales of degrees; indeed, the LVK produces combined sky maps incorporating localization information from third parties such as GRBs and neutrino alerts.[34]

Teglon can further benefit from FRB coincidences by incorporating distance constraints based on the dispersion measure obtained directly from the FRB signal. This quantity correlates directly with the column of electrons along the line of sight to the FRB; combined with information on the density of electrons in the Milky Way, host-galaxy environments, and the intergalactic medium, this electron column density can constrain the distance to an FRB (W. Deng & B. Zhang 2014; B. Zhou et al. 2014; J. P. Macquart et al. 2020). In addition to multiple independent 2D localization constraints, the Teglon algorithm can accommodate multiple independent volume localizations by combining distance distributions within each map pixel, such as replacing Equation (A.2) with a nonparametric distribution for each map pixel.

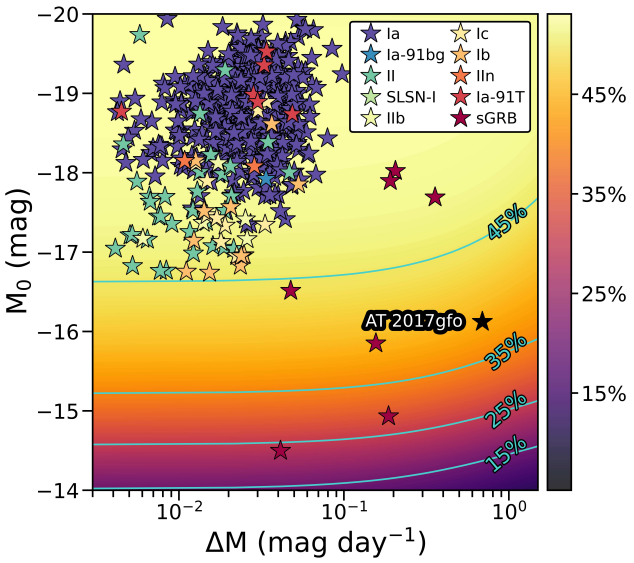

Figure 10. Similar to Figure 7 for generic linear models parameterized by a peak absolute magnitude at the time of the merger (M_0 in mag) and a linear decline rate (ΔM in mag day^{-1}) as defined by Equation (1). Our models are agnostic in their emission mechanism and have a uniform SED. We overplot a range of well-known classes of transients taken from M. R. Siebert et al. (2017) and sGRB optical *r*-, *R*-, and *I*-band emission from J. C. Rastinejad et al. (2021), as well as an average representation of AT 2017gfo ($M \approx -16$ mag, $\Delta M \approx 0.7$ mag day^{-1}; based on M. R. Drout et al. 2017; C. D. Kilpatrick et al. 2017; M. R. Siebert et al. 2017). We rule out an AT 2017gfo-like counterpart with 39.3% confidence.

[33] However, note the caveat from Section 3 that we find 28 candidates which cannot be definitively ruled out as being associated with GW190425.

[34] See https://emfollow.docs.ligo.org/userguide/content.html.

7. Conclusions

We present the most comprehensive analysis to date of UVOIR follow-up campaigns of the GW event GW190425 by the GC and publicly reported data.

1. We provide new follow-up data from the GC for GW190425, including optical and IR imaging from the KAIT, Nickel, Thacher, SMARTS 1.3 m, and Swope telescopes covering a unique 54.76 $\deg^2$ of the 90th percentile localization region and 3.99% of the `Teglon`-redistributed 2D probability (corresponding to 0.98% of the LVK-assigned 2D probability) across *uBVgriIJHK* bands. In addition, we present a new MOSFIRE IR spectrum of the high-probability candidate SN 2019ebq, demonstrating that it is consistent with an SN Ib/c at $z = 0.037$.
2. We analyze all candidate counterparts discovered within the 90th percentile localization region for GW190425, including their available spectra, possible identifications as minor planets or variable stars, host-galaxy associations and redshifts relative to the localization volume of GW190425, and photometry. We are left with 28 candidates that we cannot rule out as being associated with GW190425, four of which we consider "more likely" candidates based on their time of discovery, host-galaxy associations, and implied luminosity.
3. Assuming that none of these candidates is the counterpart to GW190425, we perform a joint analysis of our data combined with publicly reported imaging using a new tool, `Teglon`. This tool uses a 3D spatially varying galaxy catalog completeness weighting scheme, based on galaxy luminosity, to redistribute the original LVK 2D probability to account for local regions of high catalog completeness. We have provided `Teglon` (D. A. Coulter 2025, in preparation; D. A. Coulter 2021; see footnote 24) as an open-source tool available to the broader GW follow-up community. We point out that while `Teglon` offers diminishing returns for $\geqslant$1 $\deg^2$ FOV instruments, one- and two-detector events are still common owing to the varying duty cycles for ground-based GW detectors. Specifically for NS events with close-in distances and poor localizations, `Teglon` can offer an efficiency boost even for these large FOV detectors.
4. With `Teglon`, we homogeneously analyze this combined data set, covering a unique 9078.59 $\deg^2$ and 48.28% of the `Teglon`-redistributed 2D probability (corresponding to 48.13% of the LVK-assigned 2D probability) across UVOIR bands. We find that there is a 28.4% and 2.9% chance of detecting a KN similar to the blue and components (respectively) of AT 2017gfo in the combined data set. Furthermore, the data are generally insensitive to an on-axis sGRB, and we rule out a generic transient with a similar peak luminosity and decline rate as AT 2017gfo to 30% confidence. Combining new imaging data presented here as well as publicly available imaging in the literature, our `Teglon` analysis is the most comprehensive meta-analysis of GW190425 presented to date.
5. We analyze the full search for optical counterparts to GW190425 in terms of the search strategy adopted across the astronomical community, unique optical counterparts such as those arising from NS mergers in the disks of active galactic nuclei, and the possible radio counterpart FRB 190425A discovered 2.5 hr after the GW190425 merger. `Teglon` can aid in each of these cases by optimally analyzing the search strategies for multiple telescopes with varying FOV and depth, incorporating source catalogs apart from galaxies in its algorithm, and calculating the overlap between GW events and those from coincident events such as GRBs and FRBs into the localization maps that it generates.
6. Finally, while `Teglon` can optimize the search strategy (in particular for small-FOV instruments) for EM counterparts to GW events, candidate counterpart classification remains a limiting factor. Future EM searches for GW counterparts would greatly benefit from a dedicated and publicly available tool for real-time candidate vetting to optimize the precious and limited spectroscopic resources that are required to successfully identify a true counterpart to a GW event.

Acknowledgments

We appreciate the expert assistance of the staffs at the various observatories where data were obtained. We also acknowledge the important work that the Treasure Map (TM) is engaged in, by facilitating the public distribution of GW search data, which allowed this analysis to be conducted. D.A.C. thanks Leo Singer for many insightful conversations on topics as diverse as plotting to understanding GW posteriors through his comprehensive set of tools (https://lscsoft.docs.ligo.org/ligo.skymap/), Michael Coughlin for many conversations about EM search optimizations, R.H. for important conversations on the software engineering required to build `Teglon`, D.O.J. for his technical expertise in quantifying our imaging depth, Antonella Palmese for her sharp eyes reviewing equations, Stephen Smartt and I.A. for graciously sharing their pointing data with our team, Aaron Tohuvavohu and Sam Wyatt for their help integrating TM queries into `Teglon`, and Ashley Villar for her insight into `MOSFiT` modeling. D.A.C. also acknowledges support from the National Science Foundation (NSF) Graduate Research Fellowship under grant DGE-1339067.

The UCSC team is supported in part by NSF grants AST-1815935 and AST-2307710, the Gordon & Betty Moore Foundation, the Heising-Simons Foundation, and by a fellowship from the David and Lucile Packard Foundation to R.J.F. The work of P.M. was partly performed under the auspices of the U.S. Department of Energy by Lawrence Livermore National Laboratory under Contract DE-AC52-07NA27344. The document number is LLNL-JRNL-863367. I.A. is grateful for support from the European Research Council (ERC) under the European Union's Horizon 2020 research and innovation program (grant agreement 852097), from the Israel Science Foundation (grant No. 2752/19), from the United States–Israel Binational Science Foundation (BSF; grant No. 2018166), and from the Pazy Foundation (grant No. 216312). J.A.V. acknowledges the Doctorate in Astrophysics and Astroinformatics and Postgraduate School of the Universidad de Antofagasta for its support and allocated grants. E.R.-R. is supported by the Heising-Simons Foundation and the NSF (AST-2307710, AST-2206243, AST-1911206, and AST-1852393). J.S.B. is partially supported by the Gordon and Betty Moore Foundation and the NSF. M.R.D. acknowledges

support from the NSERC through grant No. RGPIN-2019-06186, the Canada Research Chairs Program, and the Dunlap Institute at the University of Toronto. A.V.F.'s research group at UC Berkeley acknowledges financial assistance from the Christopher R. Redlich Fund, as well as donations from Gary and Cynthia Bengier, Clark and Sharon Winslow, Alan Eustace (W.Z. is a Bengier-Winslow-Eustace Specialist in Astronomy), and many other individuals.

This work includes data obtained with the Swope telescope at Las Campanas Observatory, Chile, as part of the Swope Time Domain Key Project (PI: Piro; Co-Is: Burns, Coulter, Cowperthwaite, Dimitriadis, Drout, Foley, French, Holoien, Hsiao, Kilpatrick, Madore, Phillips, and Rojas-Bravo). This work makes use of data from the Las Cumbres Observatory global telescope network. The LCO group is supported by NSF grants AST-1911225 and AST-1911151, and BSF grant No. 2018166. This research has used data from the SMARTS 1.3 m telescope, which is operated as part of the SMARTS Consortium. Some of the data presented herein were obtained at the W. M. Keck Observatory, which is operated as a scientific partnership among the California Institute of Technology, the University of California, and NASA. The Observatory was made possible by the generous financial support of the W. M. Keck Foundation. The authors wish to recognize and acknowledge the very significant cultural role and reverence that the summit of Maunakea has always had within the indigenous Hawaiian community. We are most fortunate to have the opportunity to conduct observations from this mountain. Research at Lick Observatory is partially supported by a generous gift from Google. KAIT and its ongoing operation were made possible by donations from Sun Microsystems, Inc., the Hewlett-Packard Company, AutoScope Corporation, Lick Observatory, the NSF, the University of California, the Sylvia and Jim Katzman Foundation, and the TABASGO Foundation. We also appreciate data from I. Keinan & I. Arcavi (2025) shared by I.A. on behalf of Las Cumbres Observatory.

Facilities: KAIT, Keck:I (MOSFIRE), Nickel (Direct 2K), CTIO:1.3 m (ANDICAM), Swope (Direct 4K), Thacher (ACP).

Software: `astropy` (Astropy Collaboration et al. 2013, 2018, 2022), `DoPHOT` (P. L. Schechter et al. 1993), `dustmaps` (G. M. Green 2018), `healpy` (A. Zonca et al. 2019), `hotpants` (A. Becker 2015), `ligo.skymap` (L. P. Singer et al. 2016a, 2016b), `PypeIt` (J. Prochaska et al. 2020a; J. X. Prochaska et al. 2020b), `SExtractor` (E. Bertin & S. Arnouts 1996), `Teglon` (D. A. Coulter 2021), `Treasure Map` (S. D. Wyatt et al. 2020).

Appendix
Detailed Candidate Analysis

In Table 3, we classify each candidate and indicate what criteria were used to rule out its association with GW190425, following methods similar to those of C. D. Kilpatrick et al. (2021a). Of the 28 remaining candidates that we cannot rule out, we describe what is known about each source and whether it could be a viable EM counterpart to GW190425.

Several other analyses have presented a discussion of some subset of the candidate optical counterparts to GW190425 that we consider here (e.g., M. W. Coughlin et al. 2019; G. Hosseinzadeh et al. 2019; M. J. Lundquist et al. 2019; J. C. Rastinejad et al. 2022; G. S. H. Paek et al. 2024). We note that of these publications, only J. C. Rastinejad et al. (2022) report candidates that remain "viable" as counterparts to GW190425 after the cuts performed in their analysis, specifically AT 2019efr and AT 2019eig.

While we cannot rule out any of these candidates, many are unlikely to be counterparts based on some reasonable assumptions. Any candidate that has no associated host galaxy corresponding to $M < -13$ mag for the distance to GW190425 and the typical depth for optical surveys, and was discovered >5 days after merger, is considered unlikely to be the counterpart; instead, these are likely high-redshift interlopers. This results in four "more likely" candidates (AT 2019ean, 2019ego, 2019egj, and 2019aasq) that we discuss below. Finally, we conclude our analysis by considering the two high-probability counterparts reported by J. C. Rastinejad et al. (2022).

A.1. Candidate Optical Counterparts to GW190425

AT 2019ean. AT 2019ean was discovered by ZTF 0.11 days after the GW190425 merger with an initial brightness of $r = 19.87$ mag and $20''$ (12 kpc) from its likely host galaxy IC 4611 at $z = 0.029841$ (C. Fremling 2019). As shown in Table 3, it is located at the 38.8th cumulative percentile most likely part of the final GW190425 map. No additional forced-photometry detections of AT 2019ean were recovered by ATLAS or ZTF despite significant coverage by both surveys within ± 7 days of discovery. It is therefore likely that AT 2019ean peaked at $M_r \approx -15.8$ mag at the distance of its host galaxy within the first half-day of discovery, close to models of AT 2017gfo (e.g., those of P. S. Cowperthwaite et al. 2017; M. R. Drout et al. 2017; M. M. Kasliwal et al. 2017; C. D. Kilpatrick et al. 2017; S. J. Smartt et al. 2017; V. A. Villar et al. 2017). We therefore consider AT 2019ean to be a candidate KN counterpart to GW190425.

AT 2019ego. AT 2019ego was discovered by Gaia 1.80 days after the GW190425 merger with an initial brightness of $G = 18.97 \pm 0.20$ mag and $5.''1$ (3 kpc) from its likely host galaxy WISEA J004046.31–512807.8 at $z = 0.032139$ (A. Delgado et al. 2019). It is located at the 24.4th cumulative percentile most likely part of the final GW190425 map. Owing to its southern sky location at $\delta = -51.46831$ (J2000), there were limited follow-up observations at this position, hence precluding a detailed photometric classification of this event. Regardless, AT 2019ego was likely close to its peak magnitude of $M_G = -16.8$ mag around the time of discovery, and so it remains a candidate KN counterpart to GW190425 given its localization and known photometry.

AT 2019egj. AT 2019egj was discovered by the MASTER survey 3.59 days after the GW190425 merger with an initial brightness of 19 mag in a Clear filter and $12.''4$ (3 kpc) from the center of its likely edge-on spiral host galaxy SDSS J142814.30+304257.4 at $z = 0.012784$ (A. Delgado et al. 2019). It is located at the 36.5th cumulative percentile most likely part of the final GW190425 map. Despite significant coverage by ATLAS and ZTF within ± 7 days of the event, no other detections were obtained to similar depths as the discovery magnitude, and so AT 2019egj was likely close to its peak brightness of $M_{\rm Clear} = -15$ mag at the time of discovery. AT 2019egj therefore remains a candidate KN counterpart to GW190425 given its localization and known photometry.

AT 2019aasq. AT 2019aasq was discovered by the 1M2H collaboration using the Swope 1 m telescope +4.93 days after the GW190425 merger with an initial brightness of $i = 21.30 \pm 0.19$ mag and 7.″5 from the center of its likely host galaxy WISEA J154032.14+282013.7 at $z = 0.031090$ (D. A. Coulter et al. 2023), placing it close to $M_i = -14.4$ mag at the time of discovery. It is located at the 96.9th cumulative percentile most likely part of the final GW190425 map. Although ATLAS and ZTF had significant coverage of this region within ±7 days of the discovery, there are no other detections of this source, indicating that it was likely faint across most optical bands. We therefore consider AT 2019aasq as a candidate KN counterpart to GW190425.

We emphasize that while we consider these candidates to be "more likely" KNe, the implied ejecta masses based on their discovery magnitudes are large even compared with numerical relativity simulations using the component masses of GW190425. For example, in the low-spin prior scenario ($\chi < 0.05$), the expected component masses for GW190425 are $\sim 1.7\,M_\odot$ and $\sim 1.6\,M_\odot$ (R. Abbott et al. 2020b), which is expected to promptly collapse to a BH and yield $<0.01\,M_\odot$ of ejecta based on simulations from D. Radice et al. (2018). The transients we investigate would all require ejecta masses $>0.07\,M_\odot$ assuming a fixed ejecta velocity of $0.1c$ and $\kappa = 3.0$ cm^2 g^{-1}, and using the models explored in Section 5.1. Thus, while we consider these transients more likely to be counterparts to GW190425 than all other candidates in our analysis, we also consider them unlikely to be KNe.

The following two high-probability counterparts were reported by J. C. Rastinejad et al. (2022) as being viable counterparts to GW190425.

AT 2019efr. AT 2019efr has a high-probability association with a Legacy Data Release 10 (DR10) galaxy at $\alpha = 246.^\circ73420$, $\delta = 10.^\circ93818$ (J2000) whose photometric redshift is $0.38057^{+0.32302}_{-0.21038}$, placing it outside the likely GW190425 volume.

AT 2019eig. We consider AT 2019eig to be too bright at +4.3 days from merger to be a viable optical counterpart to GW190425. It has a Gaia *G*-band absolute magnitude of -18.24 ± 0.45 based on its discovery magnitude, assuming that it is located at the distance reported by its corresponding pixel in the GW190425 map (A. Delgado et al. 2019).

A.2. Model Detection Efficiencies Calculated By `Teglon`

A thorough presentation of `Teglon`'s pixel math will be presented by D. A. Coulter et al. (2025, in preparation); however, a brief treatment here will serve to contextualize our results in Section 5. To compute the efficiency with which `Teglon` detects a model given a set of observations, or "model detection efficiency," each instrument referenced in Section 2 is represented as a collection of polygons, and together with the celestial coordinates of every pointing in Table 1, uses the `healpy` library to return every pixel contained within these observations from the final localization map for GW190425. Each of these pixels contains a marginal 2D probability for the GW originating from its sky position, $P_{\mathrm{2D},i}$, as well as GW-derived distance distribution parameters, $\bar{D}_i$ and σ_{D_i}.

For each pixel i, we then retrieve the set of covering j observations (i.e., filter f and limiting magnitude $m_{j,f}$), as well as the matching absolute magnitude for a model under consideration $M_{\mathrm{model}_{j,f}}$. We combine the line-of-sight extinction (A_f; derived from E. F. Schlafly & D. P. Finkbeiner 2011), and reparameterize $m_{j,f}$ in terms of the distance $D_{\mathrm{model}_{j,f}}$ we would expect to detect a source in pixel i, as

$$_{\mathrm{model}_{j,f}} = m_{j,f} - M_{\mathrm{model}_{j,f}} - A_f \,, \tag{A1}$$

$$D_{\mathrm{model}_{j,f}} \quad [\mathrm{Mpc}] = 10^{0.2\times(\ _{\mathrm{model}_{j,f}} - 25)} \,. \tag{A2}$$

To calculate the weight of finding the counterpart, we integrate this distance distribution:

$$W_{\mathrm{model}_{i,j}} = \frac{1}{\sqrt{2\pi}\,\sigma_{D_i}} \int_0^{D_{\mathrm{model}_{j,f}}} e^{-\frac{1}{2}\left(\frac{\bar{D}_i - D}{\sigma_{D_i}}\right)} dD \,. \tag{A3}$$

To combine independent observations, we take the complement of the joint probability that we do not see the source in any epoch—that is, we weight the relative likelihood we would detect a specific model in image j with $P_{\mathrm{2D},i}$ and sum over all pixels to obtain a cumulative probability of detecting a specific model:

$$P_{\mathrm{model}} = \sum_i P_{\mathrm{2D},i} \left[1 - \prod_j \left(1 - W_{\mathrm{model}_{i,j}}\right) \right] . \tag{A4}$$

This final model detection efficiency is interpreted as the likelihood that we would have seen a source with the properties of the given model with our observations, for a wide range of models described in Section 5.

Table 3
Candidate EM Counterparts to GW190425

Name	α (J2000)	δ (J2000)	Cumulative LVK Prob.[a]	Discovery Date (MJD)	Redshift[b]	Absolute Magnitude[c] (AB mag)	Note[d]
2019ocg	16:52:45.011	−19:05:38.88	0.0923	58598.37600	0.08873 ± 0.01265 (PS1)	$r = -18.97 \pm 0.41$ (0.1 d)	(Z)
2019hae	16:55:14.932	−17:52:54.37	0.0768	58598.37600	0.07071 ± 0.00281 (PS1)	$r = -20.53 \pm 0.40$ (0.1 d)	(Z)
2019ocf	19:14:46.398	−03:00:27.02	0.8576	58598.38000	…	…	(PRE; $r = -20.31 \pm 0.43$, −166.11 d)
2019dzg	13:18:15.181	+29:40:12.98	0.8487	58598.38100	0.44779 ± 0.09683 (PS1)	$r = -22.76 \pm 0.44$ (0.0 d)	(Z)
2019oce	16:16:19.969	+21:44:27.38	0.0044	58598.39300	0.11777 ± 0.01048 (PS1)	$r = -20.97 \pm 0.40$ (0.9 d)	(Z)
…	…	…	…	…	…	…	…
2019fcu	15:51:32.943	+32:49:02.22	0.1419	58612.29653	$0.39904^{+0.16942}_{-0.11158}$ (LDR10)	$r = -22.86 \pm 0.41$ (20.1 d)	(Z)
2019flf	15:21:26.524	+37:27:16.66	0.1937	58612.30073	0.09000 ± 0.00090 (s)	$r = -19.98 \pm 0.40$ (29.9 d)	(SN) Ia
2019aasd	14:51:07.270	+52:30:03.82	0.4136	58612.30600	0.20381 ± 0.00020 (s)	$r = -21.61 \pm 0.45$ (1587.2 d)	(Z)
2019ewb	14:46:36.564	+56:14:03.12	0.3793	58612.30632	0.03824 ± 0.00004 (s)	$r = -17.59 \pm 0.43$ (20.1 d)	(Z)
2019feq	13:58:45.647	+02:50:39.14	0.8677	58612.33833	0.01635 ± 0.00002 (s)	$r = -18.30 \pm 0.40$ (336.2 d)	(PHOT; bright)

Notes. We show every candidate considered in the analysis described in Section 3. Absolute magnitudes are only given for photometry that we use to rule out candidate counterparts as described in our analysis.
[a] Cumulative probability within the `GW190425_skymap` provided by B. P. Abbott et al. (2020a).
[b] Redshifts are identified as spectroscopic (s) or photometric (by source).
[c] We indicate the absolute magnitude at our preferred redshift or the corresponding pixel in the final `GW190425_skymap` of observations used to rule out this candidate as being associated with GW190425. Where no magnitude was provided, we do not find any photometry that is inconsistent with one of our photometric models.
[d] We rule out each source based on classification as likely minor planet (MP), supernova (SN), premerger variability (VAR or PRE), a redshift inconsistent with the GW190425 volume (*Z*), or photometric evolution (PHOT) as described in Section 3.

(This table is available in its entirety in machine-readable form in the online article.)

ORCID iDs

D. A. Coulter https://orcid.org/0000-0003-4263-2228
C. D. Kilpatrick https://orcid.org/0000-0002-5740-7747
D. O. Jones https://orcid.org/0000-0002-6230-0151
R. J. Foley https://orcid.org/0000-0002-2445-5275
J. Anais Vilchez https://orcid.org/0000-0001-9051-1338
I. Arcavi https://orcid.org/0000-0001-7090-4898
K. E. Clever https://orcid.org/0000-0001-8756-1262
G. Dimitriadis https://orcid.org/0000-0001-9494-179X
A. V. Filippenko https://orcid.org/0000-0003-3460-0103
A. L. Piro https://orcid.org/0000-0001-6806-0673
P. J. Quiñonez https://orcid.org/0000-0003-4131-1676
C. Rojas-Bravo https://orcid.org/0000-0002-7559-315X
M. R. Siebert https://orcid.org/0000-0003-2445-3891
H. E. Stacey https://orcid.org/0000-0001-9316-5389
J. J. Swift https://orcid.org/0000-0002-9486-818X
W. Zheng https://orcid.org/0000-0002-2636-6508
J. S. Bloom https://orcid.org/0000-0002-7777-216X
M. J. Bustamante-Rosell https://orcid.org/0000-0003-0416-9818
K. W. Davis https://orcid.org/0000-0002-5680-4660
J. Kutcka https://orcid.org/0009-0004-7605-8484
P. Macias https://orcid.org/0000-0002-9946-4635
P. McGill https://orcid.org/0000-0002-1052-6749
E. Ramirez-Ruiz https://orcid.org/0000-0003-2558-3102
S. Tinyanont https://orcid.org/0000-0002-1481-4676
S. B. Cenko https://orcid.org/0000-0003-1673-970X
M. R. Drout https://orcid.org/0000-0001-7081-0082
R. Hausen https://orcid.org/0000-0002-8543-761X
D. Andrew Howell https://orcid.org/0000-0003-4253-656X
W. V. Jacobson-Galán https://orcid.org/0000-0002-3934-2644
D. Kasen https://orcid.org/0000-0002-5981-1022
C. McCully https://orcid.org/0000-0001-5807-7893
A. Rest https://orcid.org/0000-0002-4410-5387
K. Taggart https://orcid.org/0000-0002-5748-4558
S. Valenti https://orcid.org/0000-0001-8818-0795

References

Abac, A. G., Abbott, R., Abouelfettouh, I., et al. 2024, ApJL, 970, L34
Abazajian, K. N., Adelman-McCarthy, J. K., Agüeros, M. A., et al. 2009, ApJS, 182, 543
Abbott, B. P., Abbott, R., Abbott, T. D., et al. 2016a, PhRvL, 116, 061102
Abbott, B. P., Abbott, R., Abbott, T. D., et al. 2016b, PhRvL, 116, 241103
Abbott, B. P., Abbott, R., Abbott, T. D., et al. 2016c, LRR, 19, 1
Abbott, B. P., Abbott, R., Abbott, T. D., et al. 2016d, ApJL, 826, L13
Abbott, B. P., Abbott, R., Abbott, T. D., et al. 2017a, PhRvL, 118, 221101
Abbott, B. P., Abbott, R., Abbott, T. D., et al. 2017b, ApJL, 851, L35
Abbott, B. P., Abbott, R., Abbott, T. D., et al. 2017c, PhRvL, 119, 141101
Abbott, B. P., Abbott, R., Abbott, T. D., et al. 2017d, PhRvL, 119, 161101
Abbott, B. P., Abbott, R., Abbott, T. D., et al. 2017e, Natur, 551, 85
Abbott, B. P., Abbott, R., Abbott, T. D., et al. 2020a, ApJL, 892, L3
Abbott, R., Abbott, T. D., Abraham, S., et al. 2020b, ApJL, 896, L44
Abbott, R., Abbott, T. D., Abraham, S., et al. 2021, PhRvX, 11, 021053
Abbott, R., Abbott, T. D., Acernese, F., et al. 2023, PhRvX, 13, 041039
Abbott, T. M. C., Abdalla, F. B., Allam, S., et al. 2018, ApJS, 239, 18
Alexander, K. D., Margutti, R., Blanchard, P. K., et al. 2018, ApJL, 863, L18
Andreoni, I., Lu, W., Smith, R. M., et al. 2020, ApJL, 896, L2
Andrew, S. & Chime/FRB Collaboration 2025, ATel, 17114, 1
Annis, J., Soares-Santos, M., Strauss, M. A., et al. 2014, ApJ, 794, 120
Antier, S., Agayeva, S., Aivazyan, V., et al. 2020, MNRAS, 492, 3904
Arcavi, I., Hosseinzadeh, G., Howell, D. A., et al. 2017a, Natur, 551, 64
Arcavi, I., McCully, C., Hosseinzadeh, G., et al. 2017b, ApJL, 848, L33
Astropy Collaboration, Price-Whelan, A. M., Lim, P. L., et al. 2022, ApJ, 935, 167
Astropy Collaboration, Price-Whelan, A. M., Sipöcz, B. M., et al. 2018, AJ, 156, 123
Astropy Collaboration, Robitaille, T. P., Tollerud, E. J., et al. 2013, A&A, 558, A33
Baker, T., Bellini, E., Ferreira, P. G., et al. 2017, PhRvL, 119, 251301
Becerra, R. L., Dichiara, S., Watson, A. M., et al. 2021, MNRAS, 507, 1401
Beck, R., Szapudi, I., Flewelling, H., et al. 2021, MNRAS, 500, 1633
Becker, A., 2015 HOTPANTS: High Order Transform of PSF ANd Template Subtraction, Astrophysics Source Code Library, ascl:1504.004
Belczynski, K., Kalogera, V., & Bulik, T. 2002, ApJ, 572, 407
Bellm, E. C., Kulkarni, S. R., Graham, M. J., et al. 2019, PASP, 131, 018002
Bertin, E., & Arnouts, S. 1996, A&AS, 117, 393
Bilicki, M., Jarrett, T. H., Peacock, J. A., Cluver, M. E., & Steward, L. 2014, ApJS, 210, 9
Bochenek, C. D., Ravi, V., Belov, K. V., et al. 2020, Natur, 587, 59
Boersma, O. M., van Leeuwen, J., Adams, E. A. K., et al. 2021, A&A, 650, A131
Brown, T. M., Baliber, N., Bianco, F. B., et al. 2013, PASP, 125, 1031
Capano, C. D., Tews, I., Brown, S. M., et al. 2020, NatAs, 4, 625
Chambers, K. C., Magnier, E. A., Metcalfe, N., et al. 2016, arXiv:1612.05560
Chang, S.-W., Onken, C. A., Wolf, C., et al. 2021, PASA, 38, e024
CHIME/FRB Collaboration, Amiri, M., Andersen, B. C., et al. 2021, ApJS, 257, 59
CHIME/FRB Collaboration, Andersen, B. C., Bandura, K. M., et al. 2020, Natur, 587, 54
Christensen, E., Africano, B., Farneth, G., et al. 2018, AAS/DPS Meeting, 50, 310.10
Colless, M., Dalton, G., Maddox, S., et al. 2001, MNRAS, 328, 1039
Cook, D. O., Mazzarella, J. M., Helou, G., et al. 2023, ApJS, 268, 14
Coughlin, M. W., Ahumada, T., Anand, S., et al. 2019, ApJL, 885, L19
Coulter, D. A. 2021, Teglon: A Pixel-level Gravitational Wave Search Optimization and Analysis Code, v2, Zenodo, doi:10.5281/zenodo.5683507
Coulter, D. A., Foley, R. J., Kilpatrick, C. D., et al. 2017, Sci, 358, 1556
Coulter, D. A., Jones, D. O., McGill, P., et al. 2023c, PASP, 135, 064501
Coulter, D. A., Kilpatrick, C. D., & Foley, R. J. 2023, TNSTR, 1, 2023
Cowperthwaite, P. S., Berger, E., Villar, V. A., et al. 2017, ApJL, 848, L17
Dálya, G., Díaz, R., Bouchet, F. R., et al. 2022, MNRAS, 514, 1403
Dálya, G., Galgóczi, G., Dobos, L., et al. 2018, MNRAS, 479, 2374
Delgado, A., Harrison, D., Hodgkin, S., et al. 2019, TNSTR, 1, 2019
Deng, W., & Zhang, B. 2014, ApJL, 783, L35
DePoy, D. L., Atwood, B., Belville, S. R., et al. 2003, Proc. SPIE, 4841, 827
Dimitriadis, G., Jones, D. O., Siebert, M. R., et al. 2019, GCN, 24358, 1
Drout, M. R., Piro, A. L., Shappee, B. J., et al. 2017, Sci, 358, 1570
Evans, P. A., Kennea, J. A., Palmer, D. M., et al. 2016, MNRAS, 462, 1591
Filippenko, A. V., Li, W. D., Treffers, R. R., & Modjaz, M. 2001, in ASP Conf. Ser. 246, IAU Colloq. 183: Small Telescope Astronomy on Global Scales, ed. B. Paczynski, W.-P. Chen, & C. Lemme (San Francisco, CA: ASP), 121
Flewelling, H. A., Magnier, E. A., Chambers, K. C., et al. 2020, ApJS, 251, 7
Foley, R. J., Coulter, D. A., Kilpatrick, C. D., et al. 2020, MNRAS, 494, 190
Fong, W., & Berger, E. 2013, ApJ, 776, 18
Fong, W., Berger, E., Blanchard, P. K., et al. 2017, ApJL, 848, L23
Fong, W., Berger, E., Margutti, R., & Zauderer, B. A. 2015, ApJ, 815, 102
Fong, W., Blanchard, P. K., Alexander, K. D., et al. 2019, ApJL, 883, L1
Fong, W.-f., Nugent, A. E., Dong, Y., et al. 2022, ApJ, 940, 56
Foucart, F. 2021, in Handbook of Gravitational Wave Astronomy, ed. C. Bambi, S. Katsanevas, & K. D. Kokkotas (Berlin: Springer), 14
Fremling, C. 2019, TNSTR, 1, 2019
Gaia Collaboration, Brown, A. G. A., Vallenari, A., et al. 2021, A&A, 649, A1
Ganeshalingam, M., Li, W., Filippenko, A. V., et al. 2010, ApJS, 190, 418
Gehrels, N., Cannizzo, J. K., Kanner, J., et al. 2016, ApJ, 820, 136
Goldstein, A., Veres, P., Burns, E., et al. 2017, ApJL, 848, L14
Gompertz, B. P., Cutter, R., Steeghs, D., et al. 2020, MNRAS, 497, 726
Green, G. M. 2018, JOSS, 3, 695
Guevel, D., & Hosseinzadeh, G. 2017, Dguevel/Pyzogy: Initial Release, v0.0.1, Zenodo, doi:10.5281/zenodo.1043973
Guillochon, J., Nicholl, M., Villar, V. A., et al. 2018, ApJS, 236, 6
Haggard, D., Nynka, M., Ruan, J. J., et al. 2017, ApJL, 848, L25
Hajela, A., Margutti, R., Alexander, K. D., et al. 2019, ApJL, 886, L17
Hajela, A., Margutti, R., Bright, J. S., et al. 2022, ApJL, 927, L17
Henden, A. A., Levine, S., Terrell, D., & Welch, D. L. 2015, AAS Meeting, 225, 336.16
Hosseinzadeh, G., Cowperthwaite, P. S., Gomez, S., et al. 2019, ApJL, 880, L4
Jester, S., Schneider, D. P., Richards, G. T., et al. 2005, AJ, 130, 873

Kanner, J., Camp, J., Racusin, J., Gehrels, N., & White, D. 2012, ApJ, 759, 22
Kasen, D., Metzger, B., Barnes, J., Quataert, E., & Ramirez-Ruiz, E. 2017, Natur, 551, 80
Kasliwal, M. M., Nakar, E., Singer, L. P., et al. 2017, Sci, 358, 1559
Keinan, I., & Arcavi, I. 2025, ApJ, 985, 142
Kilpatrick, C. D. 2023, Charliekilpatrick/Candidates: Candidates v1.0, Zenodo, doi:10.5281/zenodo.8172608
Kilpatrick, C. D., Burchett, J. N., Jones, D. O., et al. 2021b, ApJL, 907, L3
Kilpatrick, C. D., Coulter, D. A., Arcavi, I., et al. 2021a, ApJ, 923, 258
Kilpatrick, C. D., Foley, R. J., Kasen, D., et al. 2017, Sci, 358, 1583
Kilpatrick, C. D., Fong, W.-f., Blanchard, P. K., et al. 2022, ApJ, 926, 49
Kilpatrick, C. D., Tejos, N., Andersen, B. C., et al. 2024, ApJ, 964, 121
Kochanek, C. S., Shappee, B. J., Stanek, K. Z., et al. 2017, PASP, 129, 104502
Kopparapu, R. K., Hanna, C., Kalogera, V., et al. 2008, ApJ, 675, 1459
Lamb, G. P., Lyman, J. D., Levan, A. J., et al. 2019, ApJL, 870, L15
Landolt, A. U. 1992, AJ, 104, 340
Law, C. J., Bower, G. C., Burke-Spolaor, S., et al. 2018, ApJS, 236, 8
Li, C. K., Lin, L., Xiong, S. L., et al. 2021, NatAs, 5, 378
Li, L.-X., & Paczyński, B. 1998, ApJL, 507, L59
Li, W., Filippenko, A. V., Chornock, R., & Jha, S. 2003, PASP, 115, 844
LIGO Scientific CollaborationVirgo Collaboration 2019, GCN, 24168, 1
Lundquist, M. J., Paterson, K., Fong, W., et al. 2019, ApJL, 881, L26
Lyman, J. D., Lamb, G. P., Levan, A. J., et al. 2018, NatAs, 2, 751
Lyutikov, M., Barkov, M. V., & Giannios, D. 2020, ApJL, 893, L39
Macquart, J.-P., Bailes, M., Bhat, N. D. R., et al. 2010, PASA, 27, 272
Macquart, J. P., Prochaska, J. X., McQuinn, M., et al. 2020, Natur, 581, 391
Makhathini, S., Mooley, K. P., Brightman, M., et al. 2021, ApJ, 922, 154
Margalit, B., Berger, E., & Metzger, B. D. 2019, ApJ, 886, 110
Margutti, R., Alexander, K. D., Xie, X., et al. 2018, ApJL, 856, L18
Margutti, R., Berger, E., Fong, W., et al. 2017, ApJL, 848, L20
McCully, C., Volgenau, N. H., Harbeck, D.-R., et al. 2018, Proc. SPIE, 10707, 107070K
McLean, I. S., Steidel, C. C., Epps, H. W., et al. 2012, Proc. SPIE, 8446, 84460J
Mereghetti, S., Savchenko, V., Ferrigno, C., et al. 2020, ApJL, 898, L29
Metzger, B. D., & Bower, G. C. 2014, MNRAS, 437, 1821
Metzger, B. D., Margalit, B., & Sironi, L. 2019, MNRAS, 485, 4091
Metzger, B. D., Martínez-Pinedo, G., Darbha, S., et al. 2010, MNRAS, 406, 2650
Moroianu, A., Wen, L., James, C. W., et al. 2023, NatAs, 7, 579
Most, E. R., Nathanail, A., & Rezzolla, L. 2018, ApJ, 864, 117
Murguia-Berthier, A., Ramirez-Ruiz, E., De Colle, F., et al. 2021, ApJ, 908, 152
Murguia-Berthier, A., Ramirez-Ruiz, E., Kilpatrick, C. D., et al. 2017, ApJL, 848, L34
Nakar, E. 2020, PhR, 886, 1
Nakar, E., & Piran, T. 2011, Natur, 478, 82
Nicholl, M., Short, P., Wiseman, P., et al. 2019, TNSCR, 1, 2019
Nugent, A. E., Fong, W.-F., Dong, Y., et al. 2022, ApJ, 940, 57
Nynka, M., Ruan, J. J., Haggard, D., & Evans, P. A. 2018, ApJL, 862, L19
Oates, S. R., Marshall, F. E., Breeveld, A. A., et al. 2021, MNRAS, 507, 1296
Oke, J. B., & Gunn, J. E. 1983, ApJ, 266, 713
Paek, G. S. H., Im, M., Kim, J., et al. 2024, ApJ, 960, 113
Panther, F. H., Anderson, G. E., Bhandari, S., et al. 2023, MNRAS, 519, 2235
Paterson, K., Lundquist, M. J., Rastinejad, J. C., et al. 2021, ApJ, 912, 128
Phinney, E. S. 1991, ApJL, 380, L17
Piro, A. L., Simon, J. D., Polin, A., et al. 2024, GCN, 36267, 1
Piro, L., Troja, E., Zhang, B., et al. 2019, MNRAS, 483, 1912
Pooley, D., Kumar, P., Wheeler, J. C., & Grossan, B. 2018, ApJL, 859, L23
Prochaska, J., Hennawi, J., Westfall, K., et al. 2020a, JOSS, 5, 2308
Prochaska, J. X., Hennawi, J., Cooke, R., et al. 2020b, Pypeit/PypeIt: Release v1.0.0, Zenodo, doi:10.5281/zenodo.3743493
Radice, D., Perego, A., Zappa, F., & Bernuzzi, S. 2018, ApJL, 852, L29
Rajwade, K. M., Bezuidenhout, M. C., Caleb, M., et al. 2022, MNRAS, 514, 1961
Rastinejad, J. C., Fong, W., Kilpatrick, C. D., et al. 2021, ApJ, 916, 89
Rastinejad, J. C., Paterson, K., Fong, W., et al. 2022, ApJ, 927, 50
Rest, A., Stubbs, C., Becker, A. C., et al. 2005, ApJ, 634, 1103
Richmond, M., Treffers, R. R., & Filippenko, A. V. 1993, PASP, 105, 1164
Ridnaia, A., Svinkin, D., Frederiks, D., et al. 2021, NatAs, 5, 372
Roberts, L. F., Kasen, D., Lee, W. H., & Ramirez-Ruiz, E. 2011, ApJL, 736, L21
Roming, P. W. A., Kennedy, T. E., Mason, K. O., et al. 2005, SSRv, 120, 95
Rosswog, S., Piran, T., & Nakar, E. 2013, MNRAS, 430, 2585
Ruan, J. J., Nynka, M., Haggard, D., Kalogera, V., & Evans, P. 2018, ApJL, 853, L4
Savchenko, V., Ferrigno, C., Kuulkers, E., et al. 2017, ApJL, 848, L15
Schechter, P. 1976, ApJ, 203, 297
Schechter, P. L., Mateo, M., & Saha, A. 1993, PASP, 105, 1342
Schlafly, E. F., & Finkbeiner, D. P. 2011, ApJ, 737, 103
Schulze, S., Tanvir, N. R. & Engrave Gw Collaboration 2024, GCN, 36274, 1
Shibata, M., & Taniguchi, K. 2006, PhRvD, 73, 064027
Shingles, L., Smith, K. W., Young, D. R., et al. 2021, TNSAN, 7, 1
Siebert, M. R., Foley, R. J., Drout, M. R., et al. 2017, ApJL, 848, L26
Singer, L. P., Chen, H.-Y., Holz, D. E., et al. 2016a, ApJL, 829, L15
Singer, L. P., Chen, H.-Y., Holz, D. E., et al. 2016b, ApJS, 226, 10
Singer, L. P., & Price, L. R. 2016, PhRvD, 93, 024013
Skrutskie, M. F., Cutri, R. M., Stiening, R., et al. 2006, AJ, 131, 1163
Smartt, S. J., Chen, T. W., Jerkstrand, A., et al. 2017, Natur, 551, 75
Smartt, S. J., Nicholl, M., Srivastav, S., et al. 2024, MNRAS, 528, 2299
Smith, K. W., Smartt, S. J., Young, D. R., et al. 2020, PASP, 132, 085002
Soares-Santos, M., Holz, D. E., Annis, J., et al. 2017, ApJL, 848, L16
Steeghs, D., Galloway, D. K., Ackley, K., et al. 2022, MNRAS, 511, 2405
Stetson, P. B. 1987, PASP, 99, 191
Swift, J. J., Andersen, K., Arculli, T., et al. 2022, PASP, 134, 035005
Tinyanont, S., Foley, R. J., Taggart, K., et al. 2024, PASP, 136, 014201
Tonry, J. L., Denneau, L., Heinze, A. N., et al. 2018, PASP, 130, 064505
Troja, E., Piro, L., Ryan, G., et al. 2018, MNRAS, 478, L18
Troja, E., Piro, L., van Eerten, H., et al. 2017, Natur, 551, 71
Troja, E., van Eerten, H., Ryan, G., et al. 2019, MNRAS, 489, 1919
Troja, E., van Eerten, H., Zhang, B., et al. 2020, MNRAS, 498, 5643
Valenti, S., Howell, D. A., Stritzinger, M. D., et al. 2016, MNRAS, 459, 3939
Valenti, S., Sand, D. J., Yang, S., et al. 2017, ApJL, 848, L24
Villar, V. A., Berger, E., Metzger, B. D., & Guillochon, J. 2017, ApJ, 849, 70
White, D. J., Daw, E. J., & Dhillon, V. S. 2011, CQGra, 28, 085016
Williams, G. G. 2018, Proc. SPIE, 10700, 107002T
Wu, Y., & MacFadyen, A. 2018, ApJ, 869, 55
Wu, Y., & MacFadyen, A. 2019, ApJL, 880, L23
Wyatt, S. D., Tohuvavohu, A., Arcavi, I., et al. 2020, ApJ, 894, 127
Zackay, B., Ofek, E. O., & Gal-Yam, A. 2016, ApJ, 830, 27
Zhang, B. 2013, ApJL, 763, L22
Zhang, B. 2023, RvMP, 95, 035005
Zheng, W., Filippenko, A. V., Mauerhan, J., et al. 2017, ApJ, 841, 64
Zheng, W., Zhang, K., Vasylyev, S., & Filippenko, A. V. 2019, GCN, 24179, 1
Zhou, B., Li, X., Wang, T., Fan, Y.-Z., & Wei, D.-M. 2014, PhRvD, 89, 107303
Zhou, R., Newman, J. A., Mao, Y.-Y., et al. 2021, MNRAS, 501, 3309
Zonca, A., Singer, L., Lenz, D., et al. 2019, JOSS, 4, 1298